

The Radial Velocity Experiment (RAVE): first data release

M. Steinmetz¹, T. Zwitter², A. Siebert^{1,3}, F. G. Watson⁴, K. C. Freeman⁵, U. Munari⁶, R. Campbell⁷, M. Williams⁵, G. M. Seabroke⁸, R. F. G. Wyse⁹, Q. A. Parker^{7,4}, O. Bienaymé¹⁰, S. Roeser¹¹, B. K. Gibson¹², G. Gilmore⁸, E. K. Grebel¹³, A. Helmi¹⁴, J. F. Navarro¹⁵, D. Burton⁴, C. J. P. Cass⁴, J. A. Dawe^{†,4}, K. Fiegert⁴, M. Hartley⁴, K. S. Russell⁴, W. Saunders⁴, H. Enke¹, J. Bailin¹⁶, J. Binney¹⁷, J. Bland-Hawthorn⁴, C. Boeche¹, W. Dehnen¹⁸, D. J. Eisenstein³, N. W. Evans⁸, M. Fiorucci⁶, J. P. Fulbright¹¹, O. Gerhard¹³, U. Jauregi², A. Kelz¹, L. Mijović², I. Minchev¹⁹, G. Parmentier⁸, J. Peñarrubia¹⁵, A. C. Quillen¹⁹, M. A. Read²⁰, G. Ruchti¹¹, R.-D. Scholz¹, A. Siviero⁶, M. C. Smith¹⁴, R. Sordo⁶, L. Veltz¹², S. Vidrih⁸, R. von Berlepsch¹, B. J. Boyle²¹, E. Schilbach¹¹

ABSTRACT

We present the first data release of the Radial Velocity Experiment (RAVE), an ambitious spectroscopic survey to measure radial velocities and stellar atmosphere parameters (temperature, metallicity, surface gravity) of up to one million stars using the 6dF multi-object spectrograph on the 1.2-m UK Schmidt Telescope of the Anglo-Australian Observatory (AAO). The RAVE program started in 2003, obtaining medium resolution spectra (median $R=7,500$) in the Ca-triplet region ($\lambda\lambda$ 8,410–8,795 Å) for southern hemisphere stars drawn from the Tycho-2

¹Astrophysikalisches Institut Potsdam, Potsdam, Germany

²University of Ljubljana, Department of Physics, Ljubljana, Slovenia

³Steward Observatory, Tucson AZ, USA

⁴Anglo Australian Observatory, Sydney, Australia

⁵RSAA, Mount Stromlo Observatory, Canberra, Australia

⁶INAF Osservatorio Astronomico di Padova, Asiago, Italy

⁷Macquarie University, Sydney, Australia

⁸Institute of Astronomy, University of Cambridge, UK

⁹Johns Hopkins University, Baltimore MD, USA

¹⁰Observatoire de Strasbourg, Strasbourg, France

¹¹Astronomische Rechen Institut, Heidelberg, Germany

¹²University of Central Lancashire, Preston, UK

¹³Astronomical Institute of the University of Basel, Basel, Switzerland

¹⁴Kapteyn Astronomical Institute, University of Groningen, Groningen, The Netherlands

¹⁵University of Victoria, Victoria, Canada

¹⁶Centre for Astrophysics and Supercomputing, Swinburne University of Technology, Hawthorn, Australia

¹⁷Rudolf Peierls Centre for Theoretical Physics, University of Oxford, UK

¹⁸University of Leicester, Leicester, UK

¹⁹University of Rochester, Rochester NY, USA

²⁰University of Edinburgh, Edinburgh, UK

²¹Australia Telescope National Facility, Sydney, Australia

[†]Deceased. This paper is dedicated to the memory of John Alan Dawe (1942-2004), Astronomer-in-Charge of the UK Schmidt Telescope 1978-1984, and enthusiastic RAVE observer 2003-4.

and SuperCOSMOS catalogs, in the magnitude range $9 < I < 12$. The first data release is described in this paper and contains radial velocities for 24,748 individual stars (25,274 measurements when including re-observations). Those data were obtained on 67 nights between 11 April 2003 to 03 April 2004. The total sky coverage within this data release is $\sim 4,760$ square degrees. The average signal to noise ratio of the observed spectra is 29.5, and 80% of the radial velocities have uncertainties better than 3.4 km/s. Combining internal errors and zero-point errors, the mode is found to be 2 km/s. Repeat observations are used to assess the stability of our radial velocity solution, resulting in a variance of 2.8 km/s. We demonstrate that the radial velocities derived for the first data set do not show any systematic trend with color or signal to noise. The RAVE radial velocities are complemented in the data release with proper motions from Starnet 2.0, Tycho-2 and SuperCOSMOS, in addition to photometric data from the major optical and infrared catalogs (Tycho-2, USNO-B, DENIS and 2MASS). The data release can be accessed via the RAVE webpage: <http://www.rave-survey.org>.

Subject headings: catalogs, surveys, stars: fundamental parameters

1. Introduction

Within the past decade it is being increasingly recognised that many of the clues to the fundamental problem of galaxy formation in the early Universe are contained in the motions and chemical composition of long-lived stars in our Milky Way galaxy (see e.g. Freeman & Bland-Hawthorn 2002). The recent discovery of several instances of tidal debris in our Galaxy challenges the view laid down in the seminal paper by Eggen et al. (1962), who envision the Galaxy to be formed in one major monolithic collapse at an early epoch, followed by a period of relative quiescence, lasting many Gyr. These examples include the discovery of the tidally distorted/disrupted Sagittarius dwarf galaxy (Ibata et al. 1994), the photometrically identified low-latitude Monoceros structure in the Sloan Digital Sky Survey Yanny et al. (2003) and the multitude of features in higher latitude fields (Belokurov et al. 2006).

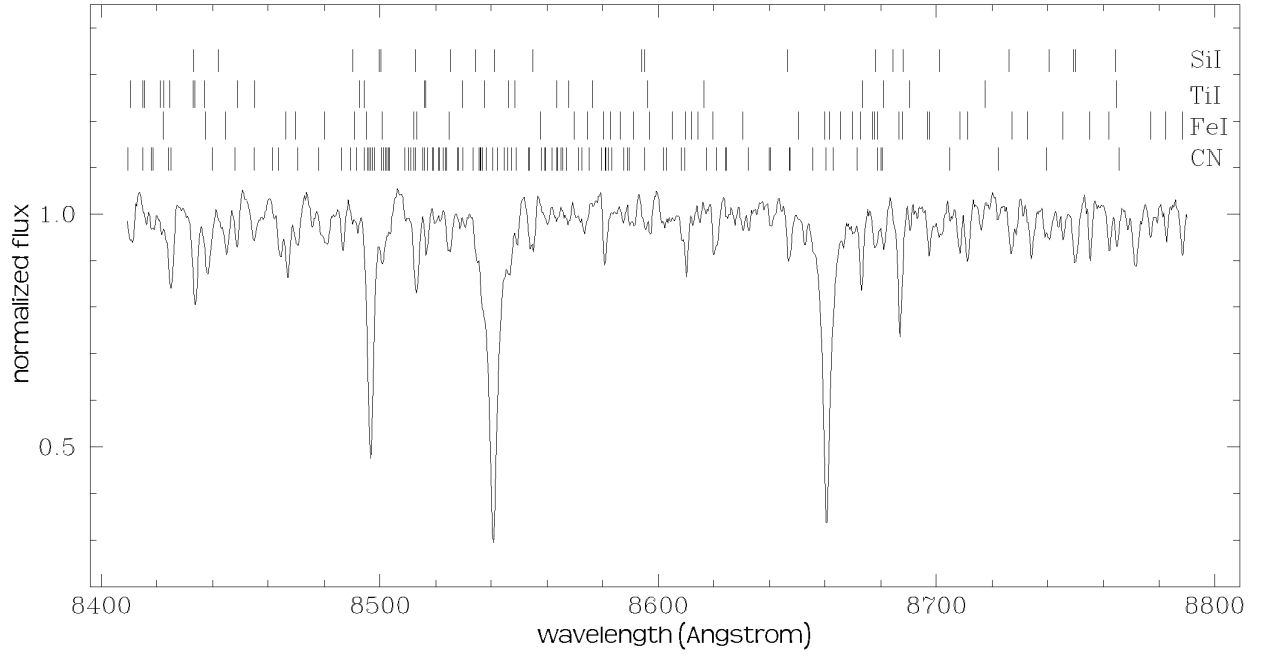


Fig. 1.— The RAVE spectrum of a typical field star, HD 154837 (K0 III), illustrating the properties of the chosen wavelength interval around the Ca II IR triplet. The strongest other absorption lines are identified.

Furthermore, within the context of the concordance Λ CDM scenario, sophisticated computer simulations of structure growth within a CDM universe have now begun to shed light on how the galaxy formation process may have taken place in a hierarchical framework (see e.g. Steinmetz & Navarro 2002, Abadi et al. 2003, Brook et al. 2005, Governato et al. 2004, Sommer-Larsen et al. 2003). These analyses lead to a reinterpretation of structures such as the Eggen moving groups (Navarro et al. 2004) or the Omega Cen globular cluster (Meza et al. 2005) in terms of merger remnants. In fact, in the extreme case, structures, and old stars, in even the thin Galactic disk are attributed to accretion events (Abadi et al. 2003; Meza et al. 2005). In addition, strong evidence for accretion and assimilation of satellite galaxies can also be seen for other galaxies in the Local Group, in particular the ‘great stream’ in M31 (Ibata et al. 2001). However, whether the Galaxy can indeed be formed by a sequence of merging events as predicted by current cosmological models of galaxy formation, or whether the few well-established accretion and merging remnants – which account for only a small fraction of the stellar mass of the Galaxy – are all there is, is still a largely unanswered question. Large kinematic surveys are needed, as are large surveys that derive chemical abundances, since both kinematics signatures and elemental abundance signatures persist longer than do spatial over-densities. It is still unclear (Wyse & Gilmore 2006), whether the observed chemical properties of the stars in the thick disk (Gilmore, Wyse & Jones 1995) can be brought into agreement with a scenario that sees the thick disk primarily as the result of accretion events (Abadi et al. 2003). A similar question arises owing to the distinct age distribution (Unavane, Wyse & Gilmore 1996, see however Abadi et al. 2003) and chemical elemental abundance distributions of stars in the stellar halo and in low-mass dwarf galaxies of the Local Group (Tolstoy et al. 2003; see however, Robertson et al. 2005, Bullock & Johnston 2005).

Stellar clusters, spiral arms, and the Galactic bar leave an imprint in the chemical and stellar velocity distribution in the solar neighborhood (Dehnen 2000; Quillen & Minchev 2005; de Simone et al. 2004) as well. Multidimensional databases are required to investigate and differentiate between these processes and structure caused by satellite accretion.

The growing awareness of the importance of the ‘fossil record’ in the Milky Way Galaxy in constraining galaxy formation theory is reflected by the increasing number of missions designed to unravel the formation history of the Galaxy. Stellar spectroscopy plays a crucial role in these studies, not only providing radial velocities as a key component of the 6-dimensional phase space of stellar positions and velocities, but also providing much-needed information on the gravity and chemical composition of individual stars. An example of the power of such multidimensional stellar datasets have recently been shown by Helmi et al. (2006) who, by using a combination of proper motions and distances from the Hipparcos catalog (ESA 1997) and spectra from the Geneva-Copenhagen Survey (Nordström et al. 2005, hereafter

GCS) were able to identify several accretion candidates within the immediate neighborhood of the Sun.

However, despite the importance of stellar spectroscopy, the past decades have seen only limited progress. Soon after Vogel (1873) measured the radial velocities of Sirius and Procyon, Seabroke (1879)¹ performed one of the first surveys, measuring 68 radial velocities for 29 stars, followed by 699 observations of 40 stars (Seabroke 1887) and 866 observations of 49 stars (Seabroke 1889). Since then, over the next 125 years, radial velocities for some 50,000 stars have become available in the public databases of the Centre de Données astronomiques de Strasbourg (hereafter CDS). This is surprisingly few, compared to the more than one million galaxy redshifts measured within the past decade. This sample of stellar radial velocities has recently been increased substantially by the GCS, containing radial velocities for 16,682 nearby dwarf stars, and by Famaey et al. (2005) publishing 6,691 radial velocities for apparently bright giant stars. Both catalogs were part of the Hipparcos follow-up campaign.

With the advent of wide field multi-object spectroscopy (MOS) fiber systems in the 1990's, pioneered particularly at the AAO with FOCAP, AUTOFIB and most recently with the 2dF and 6dF instruments on the AAT and UKST respectively (e.g. Lewis et al. 2002 and Watson et al. 2000), the possibility of undertaking wide-area surveys with hemispheric coverage became feasible. Initially, such projects were more concerned with large-scale galaxy and quasar redshift surveys (e.g. Colless et al. 2001 for 2dF and Jones et al. 2004 for 6dF). Apart from the samples of several hundred to a few thousand stars obtained prior to the commissioning of AAOmega at the AAT (see for example Kuijken & Gilmore 1989a, b, c; Gilmore, Wyse & Jones 1995; Wyse & Gilmore 1995; Gilmore, Wyse & Norris 2002) no large-scale, wide area stellar spectroscopy projects had been undertaken in our own galaxy. This has now changed with new surveys like SDSSII/SEGUE already under way, with a planned delivery of 240,000 spectra by mid 2008 (Newberg 2003), and the capabilities of AAOmega on the AAT. Over a slightly longer time frame, the RAdial Velocity Experiment (RAVE), the survey we describe in this paper, is expected to provide spectra for up to 1 Million stars by 2011. This trend for large stellar surveys will culminate with the ESA cornerstone mission Gaia, which, in addition to astrometric information, will provide multi-epoch radial velocities for up to one hundred million stars, by 2018. Each of these surveys has its own unique aspect, and they are largely complementary in capabilities and target sample.

With a radial velocity error of about 2 km/s and 80% of measurements better than 3.4 km/s, the RAVE velocities are accurate enough for almost any Galactic kinematical

¹The great-great-grandfather of G. Seabroke, co-author of this paper.

study. Radial velocities are however just one of the necessary stellar parameters: proper motions, distances and chemical abundances are also needed. Proper motions of varying accuracy are available for most of the RAVE stars, via Starnet2.0, Tycho-2 or SSS. Already, some of the cooler dwarfs ($J - K > 0.5$) with more accurate proper motions can be identified as dwarfs from their reduced proper motions. For these stars, it is possible to estimate all six phase space coordinates using their photometric parallaxes.

For most of these stars, there is no previous spectroscopic information, so the RAVE sample provides many scientific opportunities. Some of the science programs in progress by RAVE team members include:

- Discovery of extreme velocity stars and estimates of the local escape velocity and total mass of the Galaxy
- The 3D velocity distribution function of the local Galactic disk
- Kinematics of the main stellar components of the Galaxy
- Characterization of the local Galactic disk potential and the structure of the disk components
- Substructure in the disk and halo of the Galaxy, including the Arcturus, Sagittarius and other star streams
- Elemental abundances of high velocity stars
- Calibration of stellar atmospheric parameters and correspondence with the MK scheme through the HR diagram
- Searches for spectroscopic binaries and cataclysmic variables
- The $\lambda 8,620\text{\AA}$ diffuse interstellar band as an estimator of interstellar reddening.

In this paper we describe the first data release of the RAVE survey which contains radial velocities obtained from RAVE spectra (the spectra, stellar parameters and additional information will be part of the further releases as the first year spectra are contaminated by second order light). Photometric and proper motion data from other surveys are also provided for ease of use. The structure of the paper is as follows: In Section 2 we describe the survey layout, technical equipment and input catalog. Section 3 is devoted to the actual observations, followed by a section detailing the data reduction. Section 5 discusses the data quality and compares RAVE data with independent data taken with other telescopes. Finally, Section 6 provides a detailed description of the data product of the first data release (henceforth DR1) and concludes with longer term perspectives.

2. Survey design and input catalog

The wide field-of-view of the UK Schmidt and the multiplexing capability of 6dF are well-matched to a survey of apparently bright stars. The scientific goals of RAVE include analysing the chemical and dynamical evolution of the Galaxy, using as tracers both dwarfs and giants observed locally. Most apparently bright stars will be in the thin and thick disks; adopting a limiting magnitude of $I \sim 12$ (see below), dwarfs probe distances of hundreds of parsec and giants probe out to a few kiloparsec. With a sufficiently large sample, even apparently bright stars will contain a statistically relevant sample of halo stars.

The most efficient use of 6dF is when exposure times on one field matches the set-up time for the next field (see below) and this implies a limiting magnitude of around $I = 12$. As noted above, RAVE is a precursor to Gaia and the wavelength range for the RAVE spectra was chosen to match that of the Gaia Radial Velocity Spectrometer (Munari 2003, Katz et al. 2004, Wilkinson et al. 2005), namely around the Ca II IR triplet. This wavelength range also includes lines due to iron, calcium, silicon, magnesium and titanium, and detailed analyses should provide an estimate of $[\alpha/\text{Fe}]$, in addition to overall metallicity. Grids of synthetic spectra at resolution and wavelength range similar to those of RAVE, and covering wide ranges of T_{eff} , $[\text{M}/\text{H}]$, $\log g$, and V_{rot} , were calculated by Zwitter et al. (2004). and are shown in their Fig. 4.

A typical RAVE spectrum is illustrated in Fig. 1. This shows a spectrum of HD 154837 (K0 III), as observed on Sep 24 2004, with the continuum normalized to 1.0. The entire wavelength range is dominated by absorption lines; the strongest due to FeI, SiI, TiI and $^{12}\text{C}^{14}\text{N}$ are identified. The hump in the continuum around 8508 Å is produced by an opacity minimum, due in particular to the absence of $^{12}\text{C}^{14}\text{N}$ lines.

This wavelength window implies that an I -band selection is most appropriate, and this is indeed the approach taken. Star counts from the DENIS catalog to a limiting magnitude of $I = 12$ at typical latitudes and longitudes of RAVE are shown in Fig. 2 and show that a few set-ups with 6dF per line-of-sight, with a random selection over color, provide a statistically significant sample of the stars on the sky.

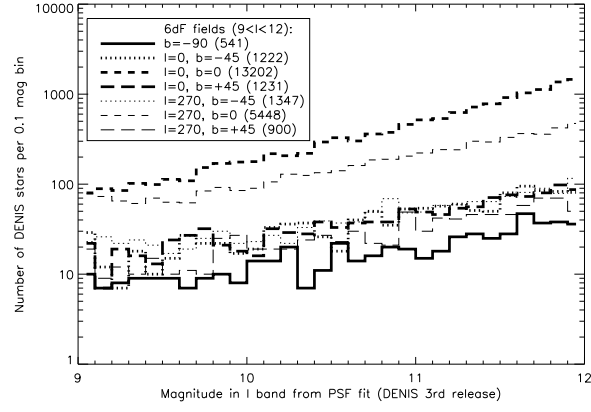


Fig. 2.— DENIS star count distributions as a function of DENIS I magnitude, using the RAVE selection criteria of $9 < I < 12$ within 6dF fields of view (5.7 degree diameter), pointing in the Galactic cardinal directions visible from the Southern hemisphere. The total number of stars matching the RAVE criteria are given in parentheses in the key to the line types.

2.1. Description of the instrument

The RAVE survey instrument is known as 6dF (Watson et al. 2000) in reference to its six degree diameter field of view. 6dF consists of an off-telescope robotic fiber positioner, two fiber-field plates of 150 fibers each and a bench-mounted spectrograph which is fed from the UK Schmidt telescope (UKST) when one of the field plates is mounted on the telescope. The light received from the target is deflected down the fiber by a 90° prism contained in a ‘button’ at the end of the fiber. This button is magnetic, allowing secure placement of the fiber on the field plate. The robot uses a pneumatically actuated gripper to pick up, and to put down, the fiber buttons. Each fiber has a diameter of $100\mu\text{m}$ (6.7 arcsec on the sky), and can be placed accurately (to within 10 microns, or 0.7 arcsec) on star positions anywhere within the 6-degree diameter field. Each field plate also contains 4 fiducial fiber bundles of 7 fibers arranged in a hexagonal pattern, which are used for field acquisition.

The bench-mounted Schmidt-type spectrograph sits on an optical bench on the floor of the telescope dome. The spectrograph therefore does not suffer from the flexure that affects telescope-mounted spectrographs which are subject to the changing gravity vector as the telescope moves across the sky. Nevertheless, it is sensitive to temperature changes (see Section 5.3). With RAVE we use a specially purchased volume phase holographic (VPH) transmission grating of medium dispersing power; this 1700 lines/mm grating is tuned for high efficiency in the I-band, and identified as grating 1700I. This setup provides in practice an average resolving power of $\sim 7,500$ over the Ca-triplet region, covering the wavelength range 8,410 to 8,795 Å.

The CCD used with the 6dF spectrograph is a Marconi (EEV) CCD47-10-BI detector. It has $13\mu\text{m}$ pixels with a $1\text{k} \times 1\text{k}$ format and is thinned and back-illuminated. The actual CCD dimensions are 1056×1027 pixels. The chip has good cosmetics, with few defects and has a quantum efficiency of 40% to 30% over the wavelength region of RAVE operations ($\lambda\lambda 8,400\text{--}8,800\text{\AA}$).

The RAVE spectrograph configuration, with the medium resolution VPH transmission grating, unfortunately exacerbates the effects of the residual aberrations within the Schmidt system. This leads to variable, position-dependent PSFs and pin-cushion distortions. Consequently, the existing pipeline reduction software, which was designed for the lower-resolution 6dF galaxy redshift survey, does not work optimally with RAVE data (but is more than adequate for quick-look, quality control purposes). A dedicated IRAF² pipeline was therefore

²IRAF is distributed by the National Optical Astronomy Observatories, which are operated by the Association of Universities for Research in Astronomy, Inc., under cooperative agreement with the National

developed for the reduction of RAVE data (see Section 4 for details).

Also most VPH gratings exhibit a ‘ghost’, due to light reflected off the detector. This ghost manifests itself as a spurious emission peak in the spectra and cannot be avoided in our RAVE observations. The wavelength of this ghost feature can be pushed into the blue part of the spectra using hardware tuning, and this wavelength region may then be excluded in the data analysis e.g. when computing the radial velocity using cross-correlation techniques. Not removing this feature properly would result in the correlation function having a strongly asymmetric profile. Fortunately, this effect is only significant in a small fraction of our spectra and this is noted by a quality flag in the corresponding entries in the data release catalog (see Appendix A Tables 5 and 7).

2.2. Instrument performance

Each field plate nominally has 150 target fibers, which when undeployed form a ring round the periphery of the 6 degree field. The fibers are evenly spaced around this ring, with the exception of two small gaps at the Northern and Southern field plate edges. Each gap creates a small ‘zone of avoidance’ which has some (small) impact on the target distributions that can be achieved. Similarly, there is a zone of avoidance, of less significance, associated with the pivot positions of each of the 4 guide fiber bundles, which are located approximately at the cardinal E-W/N-S points on each field plate. Each target fiber can nominally reach the field centre, +10%, and its deployed location relative to parked is subject to the constraint that the angle from the pure radial direction must be less than ± 14 degrees. The targets in a given input field are allocated to a given fiber using a sophisticated Field Configuration Algorithm (FCA), based on that developed for the 2dF spectrograph (Lewis et al. 2002). The FCA accepts user-supplied priorities within the input target list, but does contain subtle allocation biases, as described by Outram (2004)³ and Miszalski (2006).

These subtle allocation biases in the FCA are illustrated for the RAVE targets in Fig. 3 which shows contour plots of the successfully allocated targets, for the first year data, for each of the two field plates. The contour levels indicate the number of allocated stars per square degree. Since stars are to first order uniformly distributed across the field-of-view, the non-uniform distribution of allocated targets highlights the inherent bias in the fiber placement. The empty notches at the top and bottom of each field plate are where no fiber

Science Foundation.

³<http://www.aao.gov.au/local/www/brent/configure>.

buttons are positioned. The central under-allocated region is due to the known biases in the CONFIGURE program, by which the central region is considered easy to reach and therefore left until after harder targets, close to the field edge, have been allocated. Often this leaves fewer fibers than targets available for the centre. The remaining structure in these figures is the result of fibers being unavailable (e.g. due to breakages) or having a shorter fiber length available (after repair), re-inforcing the central deficiency.

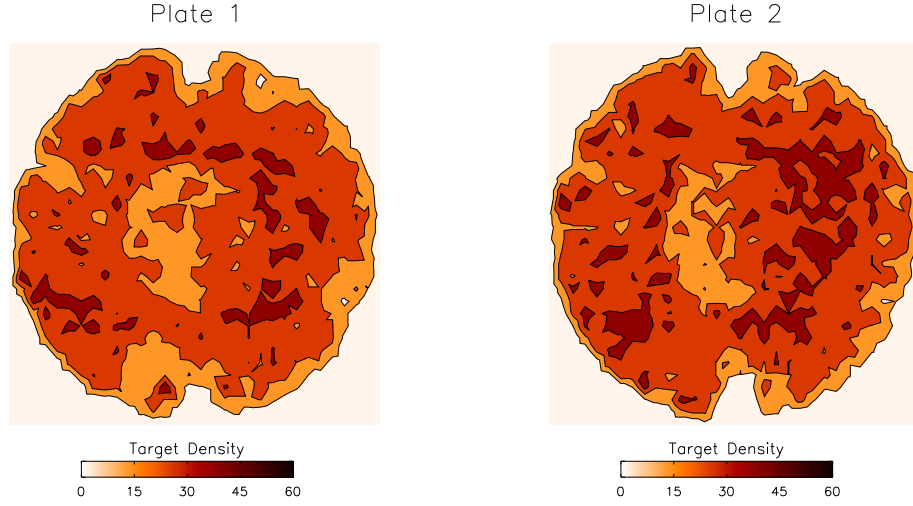


Fig. 3.— The two panels show the density of successfully allocated targets across each field plate from RAVE’s first year data. The contours are at 15, 30 and 45 allocated targets per square degree. The structure visible in each plot is due to (i) the northern and southern fiber gap across each plate, (ii) zones of avoidance around each of the 4 equally spaced guide fibers, (iii) known biases within the `CONFIGURE` program (most obvious of which is the central lefthand under-density) and (iv) broken fibers.

Over the current survey lifetime both field plates have had, on average, 130 fibers available for allocation, an extremely consistent overall level for each. The $\sim 15\%$ of fibers that are unavailable for allocation at any one time are due to a variety of causes. The most common problem is fiber breakages, that are largely the result of retractor problems on parking the fiber. Another problem is fractures in the fibers themselves (due to buttons ‘stamping’ on them during fiber placement, or having the trailing short metal shank of the fiber bent on parking, via collisions with the pivot point). Fractures may still allow light to be transmitted, but lead to severe fringing effects in any resultant spectrum. Another problem is throughput deterioration of the fibers, possibly due to a gradual clouding over time of the UV curing optical adhesive used to mate fibers to prisms (as was the case for the earlier UKST MOS system FLAIR (Parker & Watson 1990)). The final problem is related to the fiber-button gripper mechanism, which can lead to the robot being unable to pick-up or put-down some fibers.

Among the problems listed above, the first two are linked to the integrity of the fibers and can be solved by repairing them. Fiber repairs are a difficult and time-consuming process which usually involves a shortening of the fiber itself which, after several repairs, can reduce its effective range. Nevertheless considerable effort has been expended to maintain the multiplex gain of each field plate.

2.3. Sample selection and input catalog

The original RAVE sample was intended to be magnitude-limited over the range $9 < I < 12$, with no color selection (where I refers to Cousin I). At the time of the initial stages, data from the 2MASS and DENIS surveys were not yet available, and the RAVE target stars were drawn from the Tycho-2 catalog of the 2.5 million brightest stars (Høg et al. 2000) and the SuperCOSMOS Sky Survey (Hambly et al. 2001a, hereafter SSS). The Tycho observations were made in two non-standard filters, B_T and V_T . These passbands were converted to Johnson B and V using the transformation (ESA 1997)

$$\begin{aligned} V &= V_T - 0.090 (B_T - V_T), \\ B &= V + 0.850 (B_T - V_T). \end{aligned} \tag{1}$$

$(B - V)$ was transformed to I using an empirically derived zeroth-order mean color transformation derived from Bessell (1979) Tables 2 and 3:

$$(V - I) = 1.007 (B - V) + 0.03 \quad \text{if } (B - V) < 1.30,$$

$$(V - I) = 2.444 (B - V) - 1.84 \quad \text{otherwise.} \quad (2)$$

The SSS photometry (Hambly et al. 2001b) is photographic I (IVN emulsion, hereafter I_{IVN}), extracted from the SRC-I UKST IVN Survey plates by SuperCOSMOS, the automatic plate scanning facility at the Royal Observatory, Edinburgh. Blair & Gilmore (1982) showed I_{IVN} to be directly equivalent to Cousin I , essentially without any color correction, with a relation between the two magnitudes

$$I - I_{\text{IVN}} = 0.00 \pm 0.03 \times (V - I).$$

The $11 < I < 12$ interval of the first-year input catalog consists only of SSS stars. Stars with $9 < I < 11$ are mainly from Tycho-2 but also includes SSS stars that do not appear within 7 arcsec of any Tycho-2 star (this requirement is set by the 6dF fiber diameter of 6.7 arcsec). Any SSS star that does appear within 7 arcsec of a Tycho-2 star is not included, and neither is the Tycho-2 star. This procedure allows us to avoid any contamination by a possible nearby star. The quality of the photometry (not the astrometry) in both catalogs is not sufficient to discriminate between the two possibilities that either (i) the two are in fact the same star measured to have different positions in each catalog, or (ii) the two are in fact two different stars. The criteria for inclusion in the input catalog are designed to merge the two samples, taking into account both their incompletenesses at $I \sim 11$ (the faint end of Tycho-2 and the bright end of SSS) and the better proper motion accuracy provided by Tycho-2. As a result, the interim input catalog contained $\sim 300,000$ stars with $\sim 50\%$ Tycho-2 and $\sim 50\%$ SSS.

We selected 478 contiguous survey fields to cover $\sim 12,200$ square degrees of the Southern sky visible from the UKST, excluding regions with Galactic latitude $|b| < 14^\circ$, to minimize dust obscuration and crowding. The field centres are defined on a 5.7° grid spacing, corresponding to the field of view of the 6dF field plates. The gaps in between the fixed circular tiling scheme miss about 20% of the available area. For each field of view, 400 targets were randomly selected from the input catalog to construct two field files, consisting of 200 stars in each, so that at least two separate 6dF pointings could be made.

No sub-selection into bright and faint samples was made for the first 2.5 years of the RAVE survey, including the observations for this first data release. Occasionally this leads to, for example, a 9^{th} magnitude star being adjacent on the slit to a significantly fainter, 12^{th} magnitude, star. The tight spacing of the 150 fibers along the slit, as imaged onto the CCD, means that about 4% of each spectrum’s flux contaminates that of the adjacent fibers (this effect is known as fiber cross-talk). This is an insignificant problem for radial velocity determinations for the vast majority of our targets, but can impact the abundance

determinations, especially when the apparent magnitude difference between two adjacent fibers is large. This cross-talk effect is carefully taken into account by the reduction pipeline using iterative cleaning (see Section 4.2).

Typically there are ~ 200 potential targets for each field pointing at the RAVE magnitude limits which ensures efficient fiber configurations. The 6dF CONFIGURE software is usually able to allocate all the available science fibers to targets, unless two target stars are closer together than the minimum allowed separation dictated by the size of the 6dF button footprint on the field-plate (approximately 5 arcminutes). For the first year of RAVE, typically ~ 130 fibers are allocated to target stars for a single pointing. This offers scope for two pointings on some fields and re-observation of selected targets (repeats).

Both Tycho-2 and SSS are primarily astrometric catalogs and so only provide approximate photometry. The second DENIS data release, made public in 2003⁴, presented the first opportunity to compare the input catalog I directly with more accurate I -band photometry (better than 0.1 mag). As noted earlier, I_{IVN} is equivalent to standard I . Bessell (1986) showed that there is essentially no difference between Gunn- i (DENIS I) and I_{IVN} , allowing a direct comparison of input catalog I with DENIS I . Fig. 4 (top) shows that the Tycho-2 I -magnitudes derived from the Tycho-2 B_{T} and V_{T} photometry systematically agree with DENIS I (mean offset = -0.095 mag), albeit with a large scatter ($\sigma = 0.385$ mag). The SSS I -magnitudes appear to be nonlinear, systematically diverging from the DENIS I with brightness (mean offset = -0.50 mag, $\sigma = 0.33$ mag). DENIS provides the first large-scale, external check on the accuracy of the SSS photometry for bright stars. This diverging offset reflects the SSS zeropoint error in linearizing the non-linear saturation of bright stars on photographic plates. A result is that the number density of SSS stars in our sample, shown in Fig. 4 (top), actually peaks fainter than the planned selection window.

Fig. 4 (bottom) compares a subsample of observed RAVE stars with the number of DENIS stars in the same area of sky, as a function of DENIS I magnitude. The black line emphasizes that RAVE is not complete. The colored lines highlight color biases present in the input catalog. The bright sample ($I < 11$, mainly Tycho-2) has relatively more blue stars and fewer red stars than has the faint sample ($I > 11$, entirely SSS), and vice versa, reflecting the effective selection biases in the two subsamples. Although the pseudo I -band selection from Tycho-2 has reduced Tycho-2’s B -selection bias, the bias is still visible in Fig. 4, compared to real I -band selection from SSS. Hence, the input catalog is not an homogeneous selection window: sample-dependent color biases exist. In terms of stellar population studies, one of

⁴The latest DENIS release in 2005 is available at the CDS using the Vizier facility. At the time of this study, only the second incremental release was available.

RAVE’s scientific goals is to target red giants, ($1.2 < I - K \leq 1.7$), to probe the Galactic disk and halo. This goal has not been compromised by the photometry on which the interim input catalog was based.

To summarize, the catalog has no kinematic bias, but Galactic science using RAVE requires care to account for the various selection biases introduced by the inhomogeneous photometry used to derive the input sample. We must stress that the RAVE catalog in the first data release is clearly incomplete within its selection criteria (and was not intended to be complete) and has subtle color biases. The distribution of RAVE stars in the color-magnitude diagram is not entirely representative of the underlying Galactic population, due to the selection effects described above. Subsequent data releases will include stars selected by I -magnitude from the DENIS catalog, which should provide an essentially unbiased representative sample of Galactic stars in the selected range of magnitude.

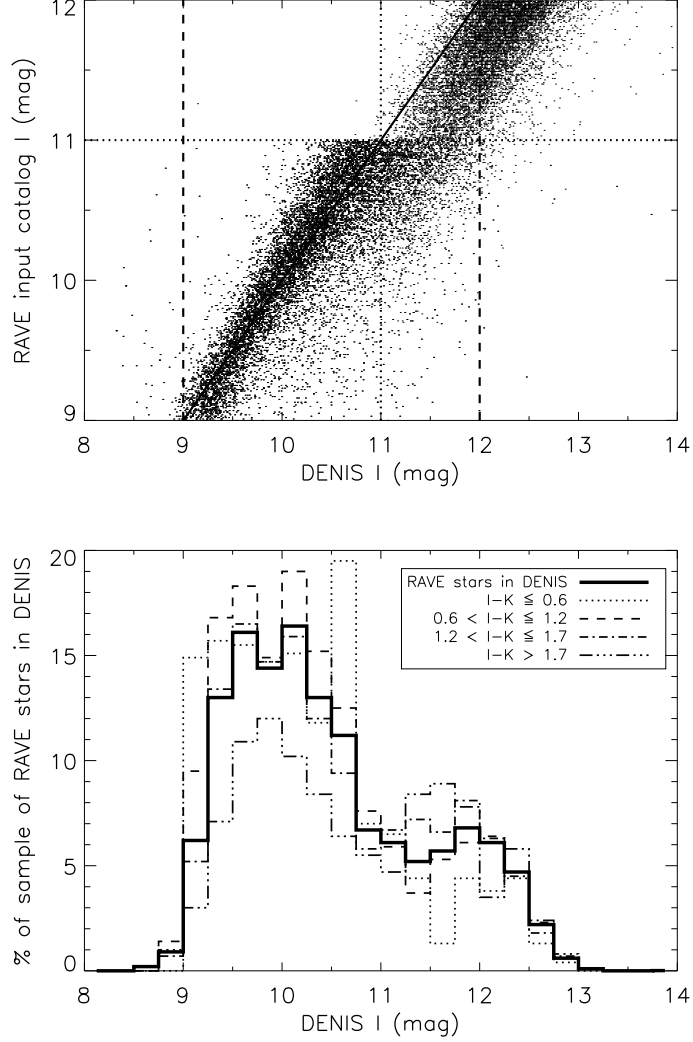


Fig. 4.— Top: Input catalog I magnitudes (Tycho-2 stars entirely within vertical axis $I < 11$ and SSS predominately within vertical axis $I > 11$) plotted as a function of DENIS I for a subsample of observed RAVE stars that are also in the second DENIS data release. The dashed lines represent the planned selection window on each axis. The dotted line delimits the bright and the faint samples at $I=11$. Bottom: Histogram of RAVE completeness compared to DENIS, as a function of DENIS I magnitude and DENIS $I-K$ color.

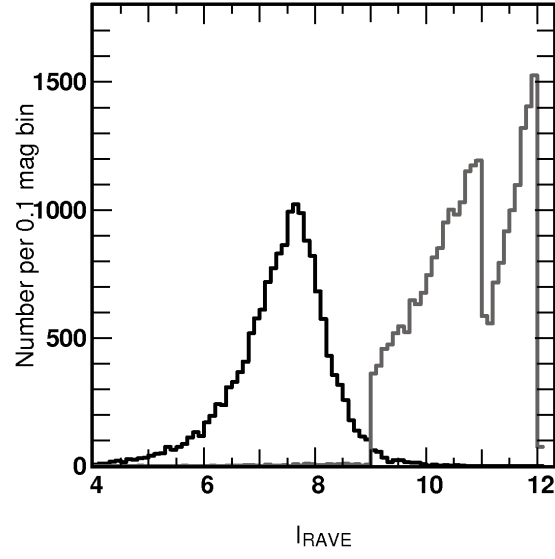


Fig. 5.— Comparison of RAVE (grey) and GCS (black) apparent magnitude distribution, showing that RAVE is significantly fainter than the previous large radial velocity survey. The GCS data (Nordstrom et al. 2004) have been transformed to RAVE’s input catalog I -band magnitude using Eqs. 1 and 2 of the text.

Fig. 5 compares the I -band apparent magnitude distributions of the RAVE sample and for the Hipparcos-based GCS sample (Nordstrom et al. 2004), which is the largest previously published sample of accurate stellar radial velocities. The RAVE I -magnitudes for the brighter RAVE stars and the GCS sample are derived from B and V magnitudes using equations 1 and 2 above. The RAVE and GCS samples hardly overlap in apparent brightness. The RAVE magnitude range ($9 < I < 12$) was chosen to match the scientific goals of the RAVE survey with the instrumental capabilities of the 6dF system. Therefore, as shown in Fig. 5, the RAVE sample is much fainter than the GCS sample. This will be relevant when we compare the RAVE velocities with those from external datasets (section 5.6).

2.3.1. RAVE Catalog contamination

Although RAVE target samples are ostensibly single stars selected from Tycho and SSS- I , both samples, including Tycho, do in fact contain double-star contaminants. This was noticed during the early part of the survey from a casual examination of printed target images. There are three main situations which arise: a) Close doubles of similar magnitude where the 6dF fiber will be positioned on the centre of the double image and a composite spectrum will result; b) Close pairs where one star is very much brighter than the other. The position for these ‘binaries’ will be heavily weighted to the bright component and so only a small effect will result; c) Relatively close pairs (and this is a situation which only arises with the SSS data at the fainter end) where a blended SSS image results but where the SSS position is between the two stars in the blend. In such cases the fiber would be positioned essentially on sky. An additional case of multiple-blends of 3 or more stars is so rare that it can be ignored. To assess the extent of the problem, 200 randomly selected fields from year 1 data were chosen and each ‘thumbnail’ small-area image for each target was carefully examined. This established that the problem was present at a maximum of 0.4% level. As a further check a blind comparison of these contaminants was made with the associated spectra to see if such blends were obvious. Only a fraction (25%) of the problem stars were obvious in the spectra. Now we have a rigorous regime where all candidate stars are checked for possible contamination prior to observing, using the 1-arcmin SSS thumbnails from the on-line SSS R -band data. Such contaminants are identified and removed from the database.

3. Observations

Observing time during the first year of the RAVE survey was confined to an average of seven bright/grey nights per lunation, distributed around (but not including) four or five

unscheduled bright-of-moon nights. The project began on 2003 April 11, and the first year’s data includes spectra obtained between then and 2004 April 3, for a total of 88 scheduled nights.

Observations for RAVE consist of a sequence of target field exposure, arc and flat. During the first year, Ne, Rb and Hg-Cd calibration exposures were obtained for each field, together with a quartz flat field for spectrum extraction in the data reduction. All calibration exposures were obtained by reflection from a white full-aperture diffusing screen located close to the entrance pupil of the telescope (the Schmidt corrector). In this position, the effects of irregularities in the screen illumination are minimised, while the fibers are illuminated at a similar focal ratio ($f/2.5$) to that of the incoming starlight. The requirement for arc and flat observations to be obtained for each field arises because the slit units are interchanged in the spectrograph for each new configuration (along with the field plates in the telescope).

Several target fibers are reserved to monitor the sky for background subtraction. As RAVE stars are quite bright, only a small fraction of the signal in each fiber comes from the sky. In most cases only sky emission lines are present, with little or no background of scattered solar spectrum from the Moon, despite the fact that most first year observations were obtained in bright or grey time. It is thus necessary to subtract this sky using measurements from dedicated sky fibers, placed uniformly across the field. A calculation of the optimal number of sky fibers per plate is given in Kuijken & Gilmore (1989b), while a detailed description of sky-subtraction with fibers is given in Wyse & Gilmore (1992). Each of the RAVE target frames therefore contained spectra of at least ten sky samples, obtained using dedicated sky fibers. These were combined and scaled in the reduction process for sky subtraction.

On a subset of nights (of order one in four), twilight exposures were also taken to provide additional zero-point velocity checks from solar absorption features and twilight sodium D lines. These were obtained with the telescope pointing towards the zenith, and taken within thirty minutes of sunset or sunrise. Those twilights frames are particularly useful to assess the zero point stability and enable some more radial velocity checks.

The target frames themselves consist of five consecutive exposures of 600 seconds each, allowing adequate signal-to-noise to be obtained in the summed spectra, while minimizing the risk of saturation from particularly bright stars. In poor conditions of low sky transparency, additional exposures are made. The total time for a ‘standard’ set of arc, flat and field exposures is of order one hour, which is similar to the fiber reconfiguration time in the 6dF robot. Thus, while observing proceeds with one field plate, the other is being re-configured, maximizing the time-on-target productivity of the telescope. Taking account of the physical transportation and exchange of the field plates, the slew time for the telescope,

field acquisition etc., an experienced observer is able to accumulate acceptable data for up to eight RAVE fields on a mid-winter’s night at the latitude of Siding Spring Observatory.

The median seeing at the focal surface of the Schmidt Telescope (i.e. including local site effects and convolved with the instrumental PSF) is ~ 2.5 arcsec. This is much less than the 6.7 arcsec diameter of the fibres, and so some seeing degradation is possible without serious loss of flux. In extremely poor conditions, however (seeing ~ 4 arcsec), there is a noticeable loss of signal. This is principally due to the difficulty in obtaining perfect target acquisition because the seeing degrades spatial resolution in the guide fibre bundles. Fortunately, such poor seeing is relatively rare (~ 10 – 15 percent of clear time).

During the first year of RAVE operations, no blocking filter was used to isolate the spectral range required, so there is second order contamination of the spectra. Flux in the approximate wavelength range $\lambda\lambda$ 4200–4400 Å is therefore added to that in the primary spectral range ($\lambda\lambda$ 8410–8790 Å). In practice, this is only a serious problem for hotter stars (earlier spectral types than $\sim F$), but features such as $H\gamma$ will be present at a low level in all stars.

The final tally for the first year’s observations was 24,748 target stars in 240 fields. Of these stars, 24,320 were observed once, 330 twice and 98 three times. A small subset of these stars (~ 100) were also observed with the 2.3-m telescope of the Australian National University at Siding Spring Observatory and the ELODIE échelle spectrograph at the Observatoire de Haute-Provence (France), and a further small number was found to be part of the GCS sample. Those observations are described in more details in section 5.6.

4. Data reduction

Data reduction for the RAVE project consists of two phases. First a quick-look data reduction is carried out at the telescope using AAO software. This was originally the 2dFdr package developed for the 2dF Galaxy Redshift Survey. It was modified to reduce 6dF data for the 6dF Galaxy Survey (therefore named 6dFdr for 6dF data reduction software). At RAVE’s high dispersion, the wavelength modelling of 6dFdr was too crude to allow arc lines to be correctly identified. Therefore, the spectrograph optics model in 6dFdr has been upgraded to allow correct line identification at all dispersions.

6dFdr was used to reduce RAVE data using simple fiber extractions from the raw data frames (summing pixel values over a fixed width around each fiber trace), without subtracting scattered light. 6dFdr was upgraded to RAVEdr in November 2004 to include scattered light subtraction. Note that RAVEdr (and 6dFdr) are able to perform more sophisticated fiber

extractions, which fit profiles to each fiber cross-section to reduce fiber cross-talk. However, this critically depends on the accurate subtraction of scattered light. The current scattered light model is only valid for all stars of equal brightness, which is not always the case for RAVE’s observations. Also, RAVE’s bright star observations cause the more sophisticated fiber extraction to be unstable so the simple method is used. This results in fiber cross-talk being not optimally modelled with RAVEdr. Therefore an IRAF-based data reduction pipeline has been built to reduce RAVE observations. This pipeline is described in section 4.1. Nevertheless, the RAVEdr reductions by the UKST observers remain useful as the first of many data quality checks.

4.1. Raw data reduction

Raw data are reduced with a custom IRAF pipeline. The pipeline uses three types of exposures to reduce every field: a set of scientific exposures is followed by a Neon arc and a flatfield exposure. The flatfield frame is used to identify the location on the CCD of the different spectra of individual fibers. This is done automatically, using the information that there are small additional gaps following the fibers with numbers 50 and 100. The pixels associated with all fibers exceeding a threshold signal are extracted. This allows the evaluation of fiber cross-talk and scattered light for any fiber with contributing light, even if it has been identified as broken.

The fibers are relatively close to each other on the CCD, with a typical fiber-to-fiber separation being approximately twice the FWHM of their spatial PSF profile. Fiber cross-talk therefore needs to be analysed and included in the reduction procedures. We adopted the following procedure: first, all light within ± 0.7 FWHM of a given fiber center is attributed to this fiber. Next, a Gaussian, modelling the contribution from the neighboring fibers, is subtracted, and then the whole procedure is iterated twice. We estimate, from our experience, that in the final spectrum less than 1% of the flux is due to stars in adjacent fibers along the slit, even if those adjacent stars are 2.5 mag brighter. This level of residual contamination is certainly acceptable.

The scattered light background requires a different careful treatment. It is relatively strong and there are no large gaps in the distribution of fibers on the entrance slit that allow for its easy determination. The scattered light is modelled by spreading a fraction of the total stellar light to a wide, axially symmetric Gaussian profile (see Wyse & Gilmore 1992 for discussion). Its width is $\sim 1/3$ of the CCD chip size and its intensity $\sim 13\%$ of the stellar flux. These two parameter values are determined iteratively by checking the residuals in flatfield and scientific exposures. Spectra of sky fibers (background) typically feature only

sky emission lines ($\sim 90\%$ of the cases), so their zero continuum value is used as a further check on the consistency of the scattered light model. In the remaining 10%, scattered light from cirrus clouds and/or moonlight add an absorption spectrum to the sky spectra (resulting in a non-zero continuum). Those cases are easily detected via the existence of Calcium absorption lines in the spectra. Here we check that the Ca lines have meaningful intensities (eg. counts at the center are non negative).

Other tasks performed by the IRAF pipeline include flatfielding, wavelength calibration, sky subtraction and heliocentric correction. Flatfielding is crucial, as fringing is very strong at the wavelengths of RAVE spectra. Wavelength calibration is achieved by a low order polynomial fit to 9 Ne arc lines. The sky to be subtracted from all spectra is determined as a median of those sky fiber spectra which are found to be free from stellar contamination, fiber cross-talk or ghost peaks.

The observed wavelengths are corrected for the rotation of the Earth, the motion of the Earth about the Earth-Moon barycenter, and the orbit of the barycenter about the Sun. The corresponding formulae are given in the help file of the procedure *rvcorrect* in IRAF. The resulting transformation from observed to heliocentric velocities should be accurate to 0.005 km/s.

A median combination of a sequence of five 600 s exposures produces the final spectrum with improved signal to noise ratio (SNR) and essentially free from cosmic ray hits (except for cosmic ray hits in the 250 s exposure of the flat field). Values of all parameters used during reduction are recorded in the reduced file’s header, while any peculiarities are noted in the appropriate reduction logs.

The procedure is automated, but the user is asked to confirm manually the crucial steps: fiber identification, scattered light subtraction parameters, quality of wavelength solution for each fiber and the appearance of fibers with sky (background) spectra. This ensures that errors due to problems with the weather or the instrument do not compromise the results. An experienced user needs ~ 20 minutes to reduce the sequence of 5 scientific exposures of a given field, together with their flatfield and arc exposures.

4.2. Radial velocity

4.2.1. Rest frame radial velocity measurement

The measurement of radial velocities is performed by an automatic pipeline (see Fig. 6 for a schematic description) which uses a standard cross-correlation procedure (Tonry &

Davis 1979). The speed of such routines, based on Fourier transforms, makes them well adapted to large datasets like RAVE where many radial velocity derivations have to be performed. Here, the pipeline uses the package XCSAO for IRAF (Kurtz et al. 1992), as it combines both the speed of the cross-correlation techniques and adequate formats for the outputs.

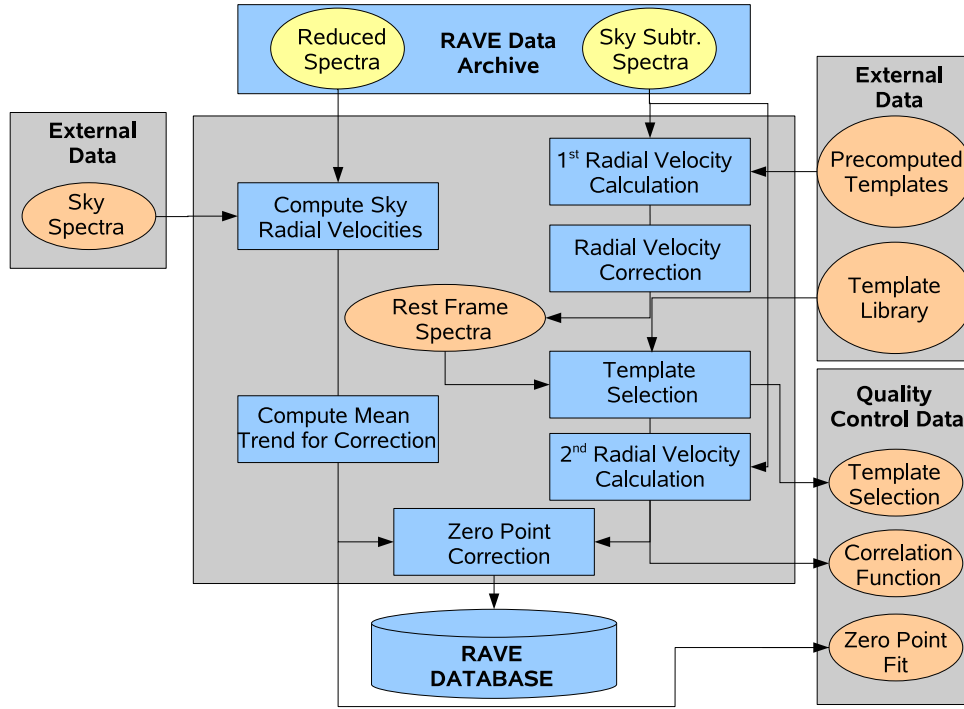


Fig. 6.— Description of the Radial Velocity Pipeline. The pipeline is made of two main branches, the first one (on the right) computes the radial velocities from sky-subtracted spectra while the second branch (on the left) uses sky unsubtracted spectra to compute the zero-point correction.

When computing the radial velocities, the blue and red ends of the spectra are rejected, the effective wavelength interval used being 8,460 Å to 8,746 Å. The reason for this is to avoid the poorer focus, lower resolving power and lower quality of the wavelength calibration at the edges of the spectral interval, while also excluding, in most of the cases, the emission ghost feature at ~ 8450 Å which was discussed in Section 2.1.

Prior to the radial velocity determination, the spectra are also continuum normalized using a cubic spline. A cosine-bell filter is used to minimize the effects of (high frequency) noise and the radial velocity is calculated by fitting a parabola to the top of the correlation peak (the top 20% of the correlation function is used throughout the pipeline).

Measuring radial velocities using cross-correlation techniques relies on the availability of accurate stellar templates to correlate with the observed spectra. Generally, one template or a reduced set of templates is used so as to match a given spectral type⁵. As the RAVE sample covers the entire color-magnitude diagram, and therefore includes large ranges of stellar physical properties such as T_{eff} , $\log g$, $[M/H]$ and rotational velocity, a large number of templates is needed in order to obtain accurate radial velocities for all targets. We use the library of theoretical spectra from Zwitter et al. (2004) covering the RAVE wavelength interval. This library contains 62,659 synthetic spectra at the RAVE/Gaia resolution, constructed using Kurucz model atmosphere code (ATLAS). It covers an extensive range of physical conditions of the stellar atmosphere.

As no blue blocking filter (OG531) was used during the first year of observations, the resulting second order contamination needs to be taken into account. The second order templates (requiring a bluer wavelength range than the Zwitter et al. spectra) are taken from the Munari et al. (2005) library, which contains 28,180 synthetic ATLAS spectra which have been degraded to RAVE’s resolution. The combination of both libraries leads to a set of 22,992 synthetic spectra that are used for this first release. The range in effective temperature of this library is $3,500\text{K} \leq T_{\text{eff}} \leq 40,000\text{K}$, giving good coverage of all spectral types. $\log g$ varies from 0 to 5 in steps of 0.5, while the metallicity $[M/H]$ is computed for $[-2.5, -2, -1.5, -1, -0.5, -0.2, 0, 0.2, 0.5]$, all scaled solar elemental abundances. The rotation velocities range from 0 km/s to 500 km/s, with irregular spacing. For the entire library of synthetic spectra, the microturbulent velocity is assumed to have the value of 2 km/s.

⁵For example, the automatic reduction pipeline for the high resolution échelle-spectrograph ELODIE at the Observatoire de Haute-Provence (used mainly for an extra-solar planet search) uses two templates, matching G and K dwarfs.

The number of template spectra is sufficiently large that it is not possible to compute the correlation function for all of them. Therefore, the radial velocities are obtained using a four-step process. In step 1, we perform a first guess of the radial velocity using a reduced set of 40 templates covering evenly the parameter space of T_{eff} , $\log g$ and 1st/2nd order ratio (matching spectral type in the template is more important for radial velocity determination than is metallicity). This first estimate provides a median internal accuracy of ~ 5 km/s for most of the CaII-dominated spectra. For early type stars, where the Paschen lines are dominant, the accuracy is lower, due to the large width of those hydrogen lines. As a comparison, the pixel size in velocity space for a typical RAVE spectrum varies from 12 km/s to 14 km/s from the red to the blue, with a mean value of 13 km/s. Therefore, with careful analysis and high SNR, we can expect to reach a ~ 1.3 km/s internal accuracy for the radial velocities (one tenth of a pixel in velocity space).

In step 2, using this first estimate of the radial velocity, the observed spectrum is shifted to the rest frame and compared to the full template database to select the ‘best-matching’ synthetic spectra. The best-matching template is defined as the spectrum (a combination of one 1st-order synthetic spectrum and one 2nd-order synthetic spectrum) which minimizes the quantity:

$$D = \sum_{\lambda} [O(\lambda) - ((1 - c)S_1(\lambda) + cS_2(\lambda))]^2, \quad (3)$$

where $O(\lambda)$ is the continuum-normalized observed target spectrum, $S_{1,2}$ are the continuum-normalized 1st and 2nd order templates and c is the fractional 2nd order contamination.

This equation does not account for a color term which is expected because of the shape of the continuum between the first-order and second-order wavelength range. Nevertheless, this effect is small (due to the limited range in wavelength of the RAVE spectra, only ~ 350 Å) compared to other sources of error, such as noise in the observed spectra or residual scattered light. Furthermore, including a color term properly would require continuum normalization for each possible combination of S_1 , S_2 and c , which is beyond the computational time limit for the pipeline. Finally, to speed up selection of the best template, c is not treated as a continuous variable, but rather is limited to discrete values between 0 and 0.8, spaced by 0.1, covering the possible values of this parameter. An example of the acceptable fit that is the outcome of this template-fitting procedure is given in Fig. 7. The estimated contribution of 2nd-order light to the observed spectrum is indicated, plus the small residuals after the template is subtracted from the observed spectrum.

At step 3, the appropriate template having been chosen, a new radial velocity is calculated. In step 4, this new determination is corrected for a possible zero-point offset. This

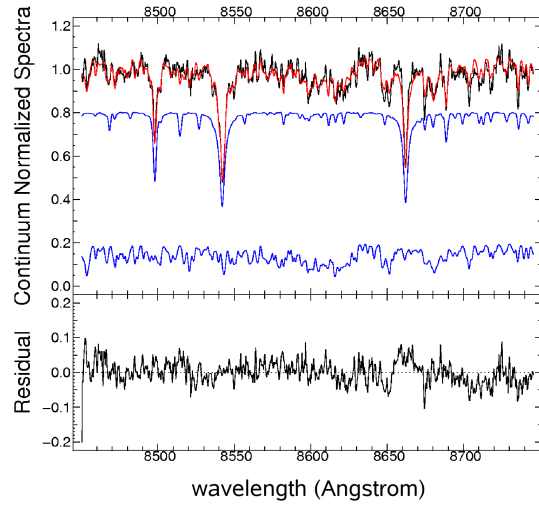


Fig. 7.— An example of the quality of the template fitting that is produced by the algorithm presented in Section 4.2, applied to the spectrum of a typical target star, here T6646_01424_1. The top panel shows the observed, continuum normalized, spectrum (in black), together with the selected template (red). The individual 1st- and 2nd-order components of the template are shown in blue. The second order contribution for this particular target amounts to less than $\sim 20\%$. The bottom panel shows the residuals after subtracting the synthetic template from the observed spectrum.

final correction, as well as its origin, are discussed in the next section.

At each of the important steps in this process the pipeline produces summary plots which are used to detect possible problems. Information from those quality-check outputs are reported in the final catalog released to the public. Also, note that the output spectra of the reduction pipeline are in the heliocentric reference frame (see section 4.1) and therefore, the radial velocities provided in the catalog are heliocentric.

4.2.2. Zero-point offset origin and correction

Analysis of raw arc frames taken before and after observations of RAVE fields showed that the positions of the emission lines in one of the arcs are sometimes shifted along the spectral axis on the CCD relative to the other arc. The origin of this shift is most likely to be temperature variations in the spectrograph room, which induce a slight change in some of the optical components. This results in a small offset in the dispersion direction, of the order of a few tenths of a pixel, between the two arc frames. This will also cause an offset between a scientific frame and the arc frame used to calibrate that science frame. The result is a zero-point offset in the measured radial velocities. A tenth of a pixel corresponds to less than 1.5 km/s, and this is then the order of the zero-point offset.

Both hardware and software were investigated to find the source of the arc shifts. The slit-vane assembly was found to be vibrationally stable, despite sharing the same mounting on the optical bench as the spectrograph shutter. The spectrograph room temperature is only recorded at the start of a RAVE setup, so the temperature change over the course of a RAVE observation is not known. Fig. 8 shows the results of an experiment to test the hypothesis that temperature variations are indeed the source of the shifts. Arc exposures were obtained over the course of a day, with the spectrograph room door shut and the dome shut. The spectrograph room temperature was recorded at the start of each arc exposure. The invar rod temperature was also recorded to check the spectrograph room thermometer. (The invar rod is within the telescope, between the primary mirror and field plate holder. Its temperature is used as an input into a model to maintain focus between the primary mirror and the field plate.) The top of Fig. 8 shows the spectrograph room thermometer is consistent with the invar rod thermometer.

The central fiber of each arc frame was extracted and cross-correlated with the central fiber of the first arc frame. The cross-correlation function (ccf) peak position corresponds to the overall emission line shift in pixels between each set of arcs. The bottom of Fig. 8 shows

a negative pixel shift trend as a result of a positive temperature change, suggesting that the spectrograph room is not a thermally stable environment and that this is responsible for the radial velocity zero-point offset.

If the glass VPH grating were expanding with temperature, the pixel shift would be positive according to the grating equation, implying that this is not the source of the zero-point shift. The thermal expansion coefficient of steel is 1.44 times that of ordinary glass but steel’s thermal conductivity is almost 63 times greater than that of glass. This suggests that various metal components of the spectrograph are temperature sensitive and thus are responsible for the zero-point shifts. Frequent monitoring of spectrograph temperature in future should improve our understanding of the zero-point shifts.

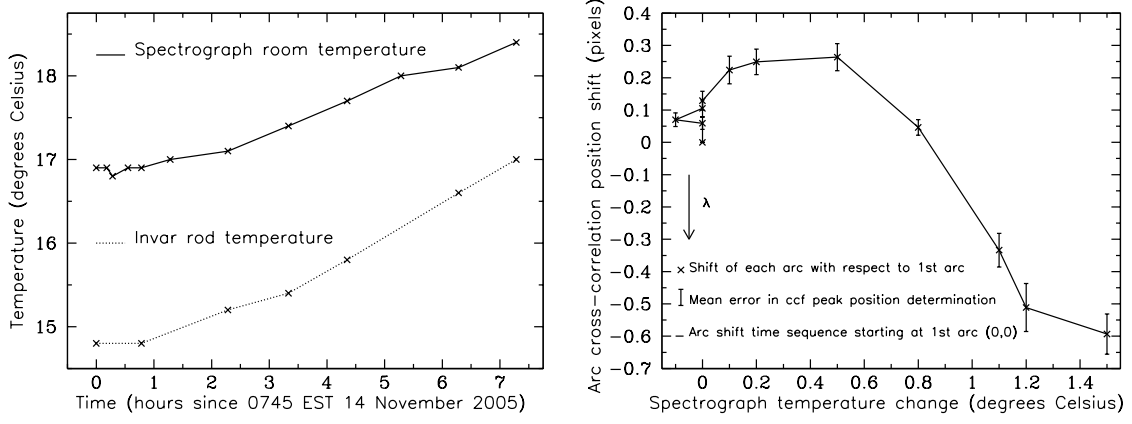


Fig. 8.— Top: Spectrograph room and invar rod temperatures as a function of time. Bottom: Shift, as a function of temperature, in the position of the cross-correlation peak for the central arc in one frame, relative to the central arc in a reference frame (the ‘1st arc’).

Given that we do not know the temperature change between a given arc frame and the observation frame to be calibrated with the arc, we need to establish the radial velocity zero-point independent of the arc frames. We therefore developed a procedure using the sky emission lines that are visible in the RAVE wavelength region. We carry out a standard cross-correlation technique with the non sky-subtracted target frames, again using the median spectrum for each fiber from the set of ≥ 5 scientific exposures. We use a sky spectrum from the Osterbrock Sky Spectra,⁶ degraded to RAVE’s resolution, as a template and compute, for each fiber, the radial velocity associated with the sky in that fiber. As the SNR for the sky lines is low, this measurement is precise only to a few km/s (the average radial velocity error for sky spectra is 6 km/s). Therefore a direct correction of a given star’s radial velocity using the measurement of the sky zero-point in the sky+star spectrum cannot be made. We instead use the fact that across a frame, the expected zero-point variation is smooth from fiber to fiber, so that a better zero-point estimation can be obtained by fitting a low-order polynomial to the {RV,Fiber} data set. Also, in order to give more weight in the fitting procedure to the dedicated sky fibers, and to the fibers containing better sky spectra (in the sense that their correlation with the template leads to more accurate velocities), the individual weight follows the Tonry-Davis R value. Further, to reject all unreliable measurements from the fit, fibers with a correlation coefficient lower than 5 are discarded. Finally, the weight for the dedicated sky fibers is doubled, to give an even stronger constraint using the fibers with no stellar spectra. Following this procedure enables us to estimate the zero point to ~ 1 km/s. An example of this calibration procedure is given in Fig. 9. The top panel shows the measured radial velocities of the sky lines and their associated errors. The thick line is the adopted polynomial fit and circles indicate the location of dedicated sky fibers. It is clearly seen that pure sky fibers have a much lower error on the determination of the radial velocity, convincing us that more weight must be given to those fibers in the fitting procedure. The bottom panel represents the array of weights used to calculate the polynomial correction for the zero point.

Fig. 10 summarizes the statistics of the applied zero point corrections. The upper panel presents their histogram with 0.1 km/s bins. The lower panel gives fraction of RAVE spectra with absolute correction lower than a given value. The absolute value of the applied zero point correction is lower than 2 km/s for 80% of the data.

⁶www-mpl.sri.com/NVAO/download/Osterbrock.html.

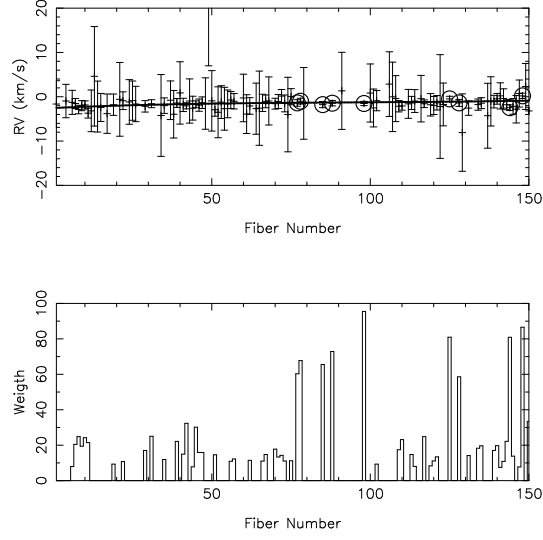


Fig. 9.— Illustration of the procedure for zero-point calibration. The top panel shows the measured radial velocity for the sky lines in each of the spectra in one RAVE field, along with their errors. Circles indicate the location of usable dedicated sky fibers (with a R value above a threshold of 5). Sky fibers with an cross-correlation R value below the limit are discarded from the fit (weight set to 0). Bottom panel: weights, proportional to the value of the Tonry-Davis R value, used by the fitting procedure. Usable dedicated sky fibers have their assigned weight doubled.

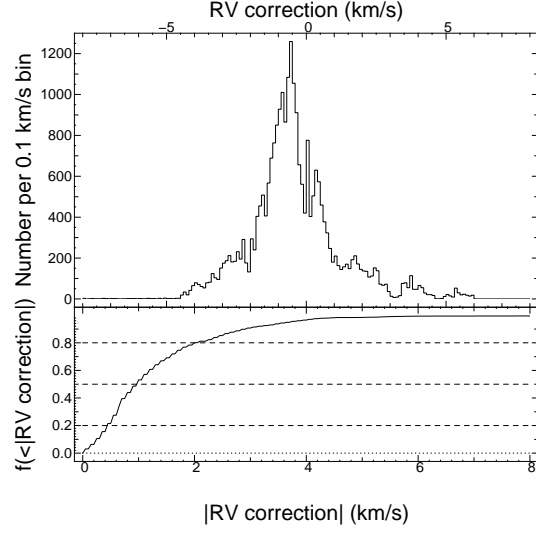


Fig. 10.— Top: histogram of the distribution of radial velocity correction due to zero-point offset. The peak value is at -0.55 km/s . Bottom: fraction of RAVE spectra with an absolute value of this correction lower than a given value. Dotted lines show limits at 20%, 50% and 80%.

5. Data quality

5.1. Signal to noise and spectral resolution

The signal to noise ratio for a given stellar spectrum was estimated from the scatter of the individual exposures in the sequence of five 10-minute exposures of a given field. At each wavelength the scatter of individual spectra scaled by their mode was determined, omitting the 2 most discordant points. This scatter then relates to the expected error of the median-combined spectrum. The reported SNR per pixel in the final extracted, one-dimensional spectrum is then calculated as an average over all wavelengths for a given star. Typical counts per pixel of the final 1-D spectrum, and per hour of exposure time, for RAVE DR1, follow the approximate relation

$$N_{\text{counts}} = 10^{-0.4(I_{\text{DENIS}} - 20.5)},$$

giving for a complete exposure $\sim 33\text{k}$ counts for an $I=9$ star and $\sim 2\text{k}$ counts for an $I=12$ star. Note that these SNR measurements, reported in Fig. 11, are conservative: the SNR in the middle of the spectral domain is generally better than the average, which is what is quoted here. Also all calculations were done on spectra that were *not* normalized. Thus a varying spectral slope and/or spectral defocusing can also worsen the reported SNR. We estimate that the accuracy of the reported SNR is $\sim 10\%$.

The resolving power $R = \lambda/\Delta\lambda$ is obtained from measurements of the width of the emission lines in the arc exposures. Near the center of the wavelength range these widths are around 3.1 pixels, which at $\lambda = 8,600 \text{ \AA}$ translates into an average resolving power $R \sim 7,500$. For stars observed with the first ~ 30 fibers the resolving power is $\sim 25\%$ lower at the edges of the wavelength range, due to spectral defocusing. These values were confirmed by fitting a large set of observed spectra of cool stars with a set of synthetic templates degraded to different spectral resolutions.

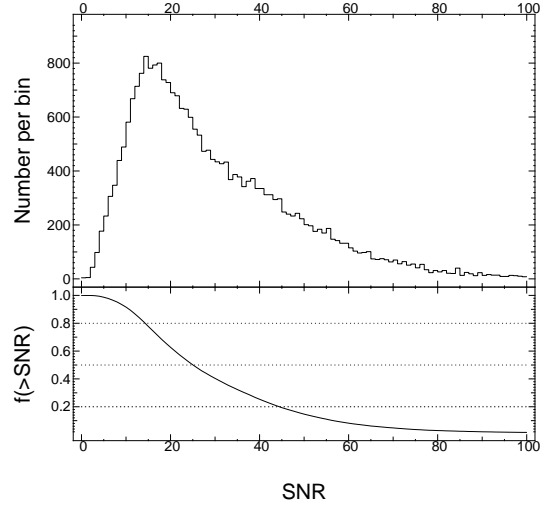


Fig. 11.— Top : histogram of the distribution of signal to noise per pixel of the final one-dimensional spectrum. The peak value is $SNR \sim 15$ while the mean value is 29.5. Bottom : fraction of RAVE spectra with SNR larger than a given value. Dotted lines show limits at 20%, 50% and 80%.

5.2. Radial velocity accuracy

As noted above, the spectra corresponding to the first data release are contaminated by second order light, due to the lack of an OG531 filter. The main effect of this contamination is that it makes it harder to model the spectra, as the amount of contamination is not known *a priori* and varies both with the spectral type and with time, as the blue to red transmission of a given fiber changes. The radial velocities, fortunately, are largely immune to this contamination by second-order light, since the location of the strong absorption lines in the first-order spectra – the primary determinations of the wavelength shift in the cross-correlation – are not affected. The contamination does lead to a poorer template match than would be achieved for pure 1st-order spectra, but again in most cases this results only in a few tenths of a km/s increase in the internal errors (as judged from repeat observations of the same star after the blocking filter was inserted, and hence without the 2nd order contamination).

The distribution of the internal radial velocity errors is presented in Fig. 12. The top panel shows the histogram of the radial velocity error in 0.5 km/s bins, while the bottom panel is the cumulative distribution. The mean internal error is 2.3 km/s, with a peak value of ~ 1.7 km/s. The bottom panel shows that more than 80% of RAVE measurements have an internal accuracy better than 3 km/s, and half of the data released reach an accuracy better than 2 km/s.

Radial velocity errors achievable for field stars of F-K spectral type have been studied during preparations for the Gaia mission. Munari et al. (2001) made observations of IAU radial velocity standards and derived the following relation for external radial velocity error in km/s as a function of SNR and spectral resolving power R

$$\begin{aligned} \log(RV \text{ error}) = & 0.6(\log SNR)^2 - 2.4 \log SNR \\ & - 1.75 \log R + 9.36 \end{aligned} \tag{4}$$

Its accuracy has been confirmed also by extensive simulations (Zwitter 2002). The error predicted for $R = 7,500$ and $SNR = 30$ (typical values for RAVE spectra) is 2.2 km/s. Relation 4 is marked by a white curve of the top-right panel in Fig. 13. The fact that RAVE performs marginally better than predicted can be traced to several factors: its wavelength range is a bit wider than for Gaia, its sampling is higher than 2 pixels per resolution element, blue order contamination contributes additional spectral lines carrying velocity information, and our SNR ratio estimate is quite conservative.

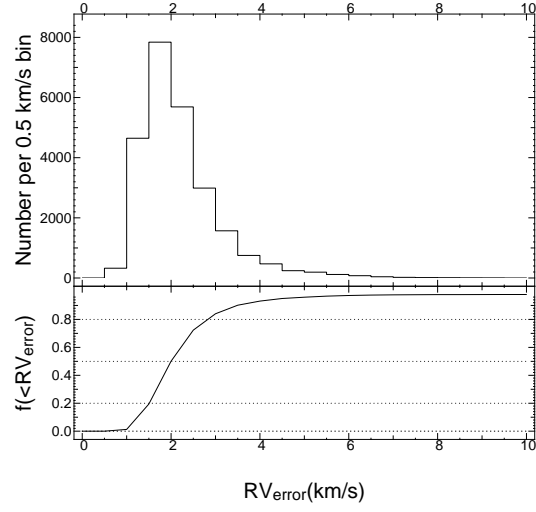


Fig. 12.— Top panel: distribution of the internal radial velocity error for RAVE DR1. The peak value is at 1.7 km/s while the average error for the catalog is 2.3 km/s. Bottom panel: fraction of RAVE targets with a radial velocity error lower than a given value. The dotted lines indicate limits of 20%, 50% and 80%.

Fig. 13 presents the relation between the radial velocity internal error and various parameters that can influence this accuracy. The upper left panel presents the 2D distribution of the radial velocity error as a function of the DENIS I -band magnitude. The color coding follows the number of objects per cell from blue (low) to red (high). It can be seen that the accuracy of the velocity determination decreases for stars with fainter I -band magnitudes. Nevertheless, there is good consistency between bright and faint targets, with the peak value of the error varying only from ~ 1.4 km/s to ~ 2 km/s between $I = 9$ and $I = 12.5$. The increase in scatter to fainter magnitudes reflects the generally lower signal-to-noise at these magnitudes, as seen in Fig. 14; the average signal-to-noise is ~ 10 for the faintest stars and ~ 70 for the brightest ones. It should be noted that the velocities for the vast majority of the stars, even at the faint limit, remain very accurate.

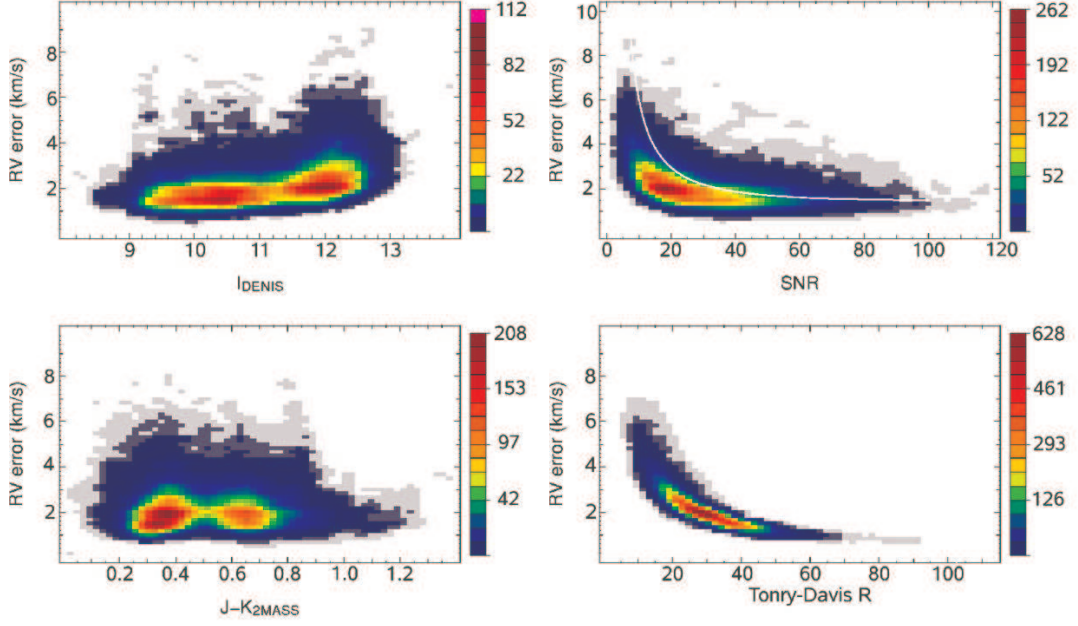


Fig. 13.— 2D histograms of the distribution of the radial velocity internal error. The color coding follows the number of objects per cell, from blue to red. Top left : as a function of I magnitude; top right : signal to noise ratio – the white line follows equation 4; bottom left : $J - K$ color; bottom right : Tonry-Davis cross-correlation R value.

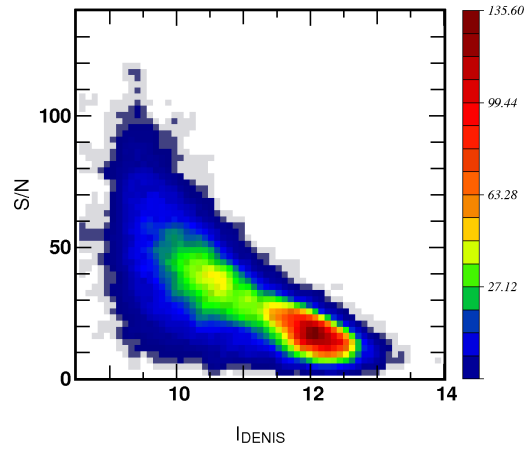


Fig. 14.— Signal to noise ratio vs DENIS I for RAVE spectra. Again the color coding follows the number of object per bin.

The effect of Poisson noise is more clearly seen in the upper right panel of Fig. 13 where the internal radial velocity error is presented as a function of the signal to noise. This shows that the errors are stable above a threshold value in SNR of around 20, while below this value, the velocity errors increase. To quantify the effect, the median value of the internal error, per bin of size 10 in SNR, varies by only 0.3 km/s (peak to peak) above SNR=20, while the lowest two bins respectively are larger by 1.1 km/s and 0.5 km/s. This is also seen in the bottom right panel, as the radial velocity error clearly drops as the cross-correlation R coefficient decreases. Finally, the bottom left panel presents the distribution of the radial velocity error as a function of the $J - K$ color. No clear variation for the peak value is seen in this diagram, but again there is some increase in scatter from red to blue. This is due to the emergence of the wide Paschen lines in the spectra of early-type stars, and the correspondingly wider correlation function peak.

5.3. Accuracy of the zero point in radial velocity

The discussion above concerned the internal accuracy of the radial velocities. As mentioned in Section 4.2.2, the radial velocity pipeline also corrects the measurements for zero point offsets. This correction is computed for each spectrum using a fit to velocities derived from the sky emission lines. This process is of course not exact and adds a further error term which must be taken into account when using the RAVE catalog. The combined error (zero-point error + internal error) on the radial velocity is discussed later when comparing RAVE radial velocities to external data (see section 5.6).

The accuracy of the zero-point correction is summarized in the DR1 catalog in the ZEROPOINTQUALITYFLAG (see Appendix A). This flag is built using a succession of three characters. The first character describes the dispersion between the measured sky radial velocities and the adopted correction (using the fibers that were used for the fit) for the complete field (therefore a field flag). This character ranges from A to E and the corresponding dispersion intervals are reported in Table 1. As the quality of the fit for an individual spectrum may depend on the location on the CCD, the field is divided in three equal parts according to the fiber number (fiber 1–50, 51–100 and 101–150) and the dispersion is computed for each sub-group of fibers (group flag in Table 2). The second character in the flag summarizes the dispersion for the group to which the fiber belongs (using a flag value from A to D in Table 1). Finally, if the interval between two successive fibers with usable sky velocities is larger than 15 fibers, the zero point correction may not be well constrained, even without the value of the dispersion being high. For those targets, the last character of the flag is set to ‘*’, indicating a possible zero-point calibration problem.

Table 2 summarizes the fraction of targets with a given flag value for each part of the zero-point correction. Over 97% of the RAVE targets have a zero-point calibration accurate to better than 2 km/s, $\sim 73\%$ to better than 1 km/s. From those numbers we can conclude that our procedure to correct from zero-point offset is efficient, enabling us to keep the zero-point error term below 2 km/s for the vast majority of our targets.

Adopting a zero-point error of 1 km/s, the mode of the radial velocity error distribution for the RAVE DR1 catalog is 2 km/s.

5.4. Repeated observations

A total of 428 stars in the present data release were observed more than once during the first year of operation. Of these, 98 stars were observed three times.

Assuming that any variation of the measured radial velocities is not intrinsic, one can thus estimate the accuracy of the catalog. The distribution of the derived radial velocities of the repeat observations is shown in Fig. 15. The mean deviation is essentially zero, and the rms of 2.83 km/s is perfectly consistent with the internal error and zero-point accuracy given above.

Table 1. Description of the zero-point quality flag.

Flag Value	Dispersion
A	0 km/s $< \sigma <$ 1 km/s
B	1 km/s $\leq \sigma <$ 2 km/s
C	2 km/s $\leq \sigma <$ 3 km/s
D	3 km/s $\leq \sigma$
E	Less than 15 fibers available for the fit

Table 2. This table presents a summary of the zero point quality flag frequency distributions in RAVE first data release for each flag group (see text).

Field Flag				
A	B	C	D	E
73.7%	23.7%	1.1%	0.4%	1.1%
Group Flag				
A	B	C	D	
73.8%	23.8%	1.8%	0.6%	
Possible Bad Calibration				
*				
3.7%				

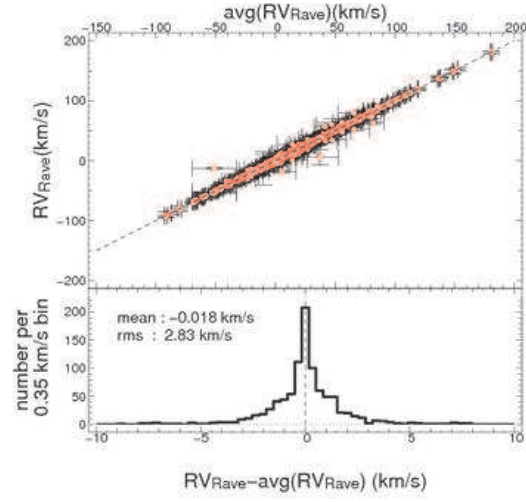


Fig. 15.— Radial velocity accuracy checked by repeated observations of 428 stars. The scatter of 2.83 km/s is consistent with estimates of internal and zero-point RV errors.

5.5. Contamination by binary stars

Most of the stars in the present data release are observed only once, so we have no way of knowing whether a given star is single, or whether the observed radial velocity may in part reflect the instantaneous radial component of the orbital motion in a binary system. The average orbital velocity of star 1 in orbit around star 2 is

$$\langle V_{\text{orb}} \rangle = v_o q (1 + q)^{-1} (M/P)^{1/3},$$

where $v_o = 30 \text{ km s}^{-1}$, $q = M_2/M_1$ is the mass ratio, and M , P are the total mass and orbital period, expressed in solar masses and years for the resultant velocity in km/s. Thus for most single-lined systems, with an orbital period of years or less, the orbital radial velocity projection exceeds 5 km/s and their kinematic data may be inaccurate and even potentially misleading. This is consistent with the 15 km/s value for the average scatter of individual radial velocities of spectroscopic binaries found by Nordström et al. (2004). Note that these authors made many repeat observations and identified 19% of their sample as spectroscopic binaries of some kind. Double-lined systems show asymmetric, or even double-peaked, shapes of the correlation function. The present release contains 27 targets flagged as possible binaries since they show clear asymmetric profiles for the correlation function as well as poor template match, or clear double-line spectra. Nevertheless, we cannot unequivocally state these are binaries without temporal orbital variations to the radial velocities, as non-intrinsic effects (for example scattered light residual or fiber cross-talk) could also contribute. Therefore this information should be used with caution.

Photometric variability is an efficient way to discover binary systems with periods of hours or days (Piquard et al. 2001), while systems with periods of hundreds of years are spatially resolved (see Figs. 3 and 4 from Zwitter & Munari 2004). Unfortunately no repeated photometric observation or light curves are available for stars in this data release. A cross-check with the general catalog of variable stars (Samus et al. 2004) revealed 22 matches. Those objects are flagged in the catalog using the VARFLAG entry (see Appendix A). While every effort has been made to identify visual binaries from available catalogs, as well as at the telescope, we note that the amplitudes of the orbital velocities of member stars of such systems is very small, and indeed less than our internal accuracy, so would not affect our quoted radial velocity values.

In future years repeats will be obtained for a larger fraction of stars, including some of the stars from this data release. This will help to identify spectroscopic binaries and active stars.

5.6. Comparison with external datasets

To further check the consistency of our radial velocities, we compare our measurements with external data from three main sources⁷: dedicated observations using the ELODIE spectrograph; dedicated observations using the MSSSO 2.3m telescope; overlap with the sample of the Geneva-Copenhagen survey (GCS). Each sub-set will be briefly described below.

ELODIE data:

ELODIE is a cross-dispersed échelle spectrograph mounted at the Cassegrain focus of the 1.93m telescope at the Observatoire de Haute Provence. The spectra cover a 3,000 Å wavelength range (3,850–6,800 Å) with a spectral resolution of 42,000. The instrument is entirely computer controlled and a standard reduction software package (TACOS) automatically processes the data. Seven stars of this first release, selected simply to be bright and accessible, were observed on three nights in July 2004 (July 5, 8 and 9). The SNRs of the spectra range from 1 to 5 per pixel (10 to 20 minutes of exposure time), sufficient at these high spectral resolutions⁸. We cross-correlated the spectra against the most appropriate spectral template given by the ELODIE reduction pipeline⁹. The results are given in Appendix B Table 8. The limiting accuracy ranges from 300 m/s to 1 km/s, with the exception of the probable double star (TYC 5031_478_1) that has been discarded from the analysis. From the six single stars measured with ELODIE for this release, we obtained a dispersion $\sigma(RV_{\text{ELODIE}} - RV_{\text{RAVE}}) = 1.7$ km/s, dominated by errors in the RAVE measurements. We find a negligible offset with the mean being $\langle (RV_{\text{ELODIE}} - RV_{\text{RAVE}}) \rangle = -0.1 \pm 0.8$ km/s, showing that the final zero-point error for RAVE data is much smaller than the measurement dispersion.

2.3m data:

Long slit spectra were taken with the Double Beam Spectrograph (DBS) (Rodgers et al. 1988) on the MSSSO 2.3m telescope, over a period of two years from December 2003 to

⁷A few stars from this release were also observed with the echelle spectrograph at the APO 3.5m telescope, as part of a follow-up scientific project. They will be published as part of the science paper.

⁸An accuracy of 10 m/s can be reached for planet searches using this instrument.

⁹TACOS provides two templates, the first one R37000K0 is valid for G, K and M stars while R37000F0 is used for spectral types around F0.

September 2005. The average seeing was $1.5'' - 2.5''$, where a narrow slit ($1.5''$) minimized slit positioning errors. The spectral resolution is similar to RAVE ($R \sim 8,000$) with $0.55 \text{ \AA}/\text{pix}$. The stars, randomly selected from the first year of observation with the exception of a few high-velocity candidates, were observed at a vertical angle of 0° or 180° to eliminate atmospheric dispersion effects. The average SNR was ~ 90 per pixel. We cross-correlated these spectra against a sub-set of the Zwitter et al. (2004) spectra using XCSAO in IRAF. The best match was chosen as the template with the highest R coefficient (Tonry & Davis 1979). Only those stars with a best-match $R > 40$ were used - this limit was found empirically to minimize errors in 2.3m radial velocities. The resulting internal error of the 2.3m radial velocities from these methods, measured against high-precision Nordström et al. stars and radial velocity standards, is $\sim 1.5 \text{ km/s}$. The results are given in Appendix B Table 9.

The 77 stars belonging to this data release and measured with the 2.3m telescope cover a radial velocity range of 820 km/s . Of those, we believe 7 outliers are likely single-lined spectroscopic binaries, as the difference in radial velocity between the RAVE and 2.3m measurements deviates by over 3σ . Excluding these 7 outliers, we find $\sigma(RV_{2.3m} - RV_{\text{RAVE}}) = 3.4 \text{ km/s}$ and $\mu(RV_{2.3m} - RV_{\text{RAVE}}) = 0.1 \pm 0.4 \text{ km/s}$. Correcting for 2.3m internal error we conclude from this sample that the RAVE radial velocity error is $\sigma = 3.0 \text{ km/s}$, with a negligible mean offset.

Geneva-Copenhagen targets:

DR1 targets have been cross-matched with the GCS catalog, which by virtue of many repeated observations contains binarity indicators in addition to accurate radial velocities. We found 13 matches, two of them classified as binaries in the GCS.

The resulting 11 ‘single’ targets show acceptable agreement with a mean difference of $1.4 \pm 0.4 \text{ km/s}$ and a rms of 1.4 km/s . The results are given in Appendix B Table 10.

Figs. 16 to 19 summarize the comparison of RAVE RVs with the external data. Fig. 16 shows the location in the 2MASS color-color diagram of the RAVE targets with external measurements. The broad distribution of those objects in this diagram indicates that we have good coverage of the global stellar properties, with the exception only of the reddest giants ($H - K \gtrsim 0.2$). Our external checks should therefore be applicable to the full survey, despite the low number of external targets.

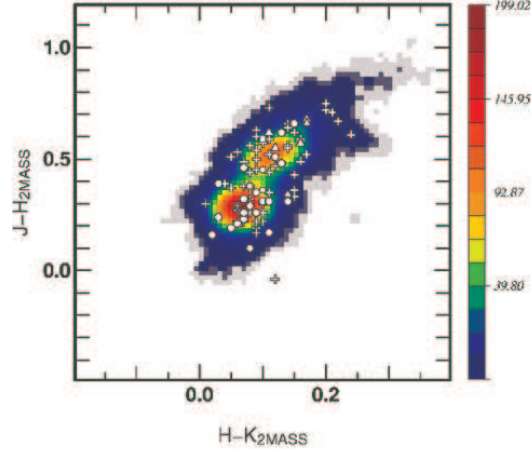


Fig. 16.— Infrared color-color diagram of the stars in DR1. The locations of our targets with external data are overplotted using white symbols. Crosses are for 2.3 m data, triangles for ELODIE targets and squares for GCS targets. Open circles denote the location of binary targets. The external targets are well-distributed across this parameter space, indicating that our reference target selection is not biased towards any particular type of objects.

Fig. 17 presents the comparison between the RAVE radial velocities and the external measurements. The top panel shows the RV to RV comparison, each different source plotted with different symbols (open circles are for binary systems that are removed from the analysis). For each data source, the mean difference and standard deviation is also given. As the spread in radial velocity is large, the bottom panel gives the radial velocity difference as a function of RV. This plot clearly shows that the binary systems produce a large offset, while single stars show good agreement, with close to zero velocity difference. We concluded in Section 5.3 that the mode is 2 km/s, the median RAVE error being ~ 2.2 km/s. Combining the measurements from all three samples, the mean difference between RAVE radial velocities and external measurements is -0.04 ± 0.29 km/s with a standard deviation of 3 km/s¹⁰. This is in good agreement with our predicted accuracy.

¹⁰The standard deviation corrected for external source mean error is $\sigma = 2.7$ km/s.

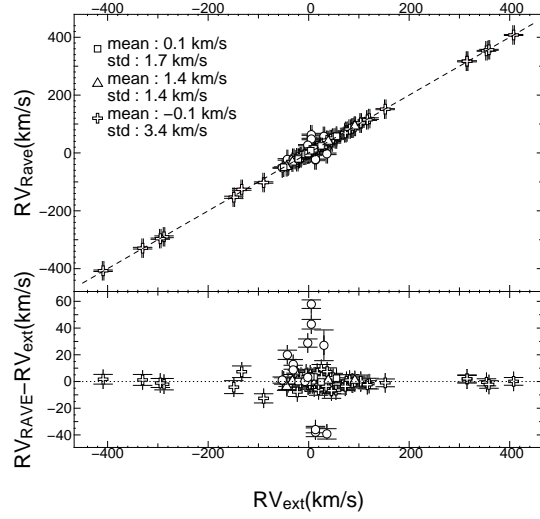


Fig. 17.— Comparison of RAVE radial velocities with external measurements. The top panel presents the external to RAVE radial velocity comparison. The bottom panel shows the radial velocity difference as a function of radial velocity for the three different reference groups. Squares are for ELODIE, triangles for GCS and crosses for 2.3 m targets. Open circles denote suspected and confirmed binary objects and are removed from the analysis. The mean difference and standard deviation are reported for each group in the top panel. RAVE radial velocities show a good agreement with independent measurements.

As a further test, we compare in Fig. 18 the radial velocity difference to the SNR in RAVE data. The top panel in this figure is a simple scatter plot including all available data, while the bottom panel presents the mean difference and rms for intervals of 10 in SNR. The offset in the interval $50 \leq \text{SNR} < 60$ is due to a single measurement with large error and RV difference ($\text{RV}_{diff} = 7 \pm 5$ km/s). This figure shows no dependence of the radial velocity on SNR, the mean and rms being consistent with no trend. Again, the amplitude of the scatter increases as the SNR drops below ~ 20 , as expected from the top right panel of Fig. 13.

Finally Fig. 19 demonstrates that radial velocity errors do not depend on color. The exception are the bluest of our targets ($J - K < 0.1$) which are dominated by wide hydrogen lines with only a handful of weak metallic lines.

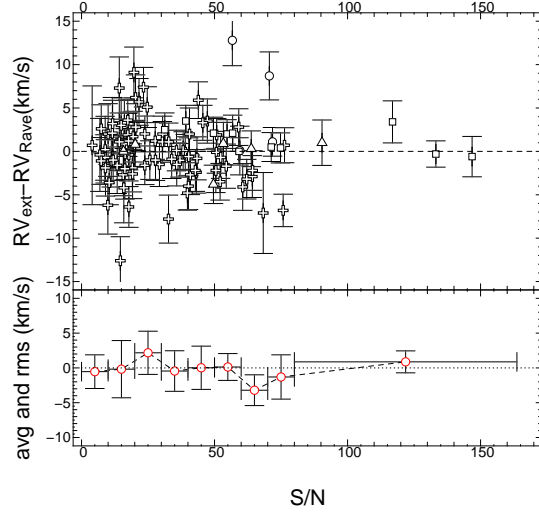


Fig. 18.— Behaviour of the radial velocity difference with signal to noise. Top panel : radial velocity difference as a function of signal to noise for each group of external measurements. Symbols are as in Fig. 16. Bottom panel : average deviation and rms as a function of signal to noise for the sum of all external measurements. This plot shows no apparent bias as a function of SNR, the mean difference being consistent with zero for all values of SNR. One bin ($60 < \text{SNR} < 70$) has a rather large deviation due to one single object with large error.

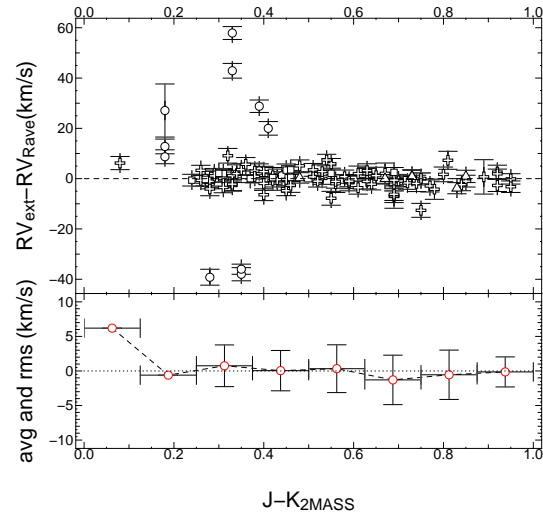


Fig. 19.— Behaviour of the radial velocity difference with $J - K$ color from the 2MASS catalog. Arrangement and symbols as in Fig. 18. Radial velocity errors do not depend on color of the target except for the bluest targets.

In summary, a comparison of the RAVE velocities with those from the three external sources (ELODIE, GCS and 2.3-m) reveals that the offset in mean velocity is very small, most likely less than 1 km/s. The errors in the RAVE stars in common with the ELODIE and GCS observations are 1.7 and 1.4 km/s respectively, while the corresponding error in the RAVE velocities of 2.3-m stars are larger, about 3.0 km/s. We note that the ELODIE and GCS stars are significantly brighter in the mean than the 2.3-m stars (see Fig. 5). However, Fig. 18 shows that the difference in estimated errors is probably not due to different SNR values for the RAVE spectra. A more likely explanation is that the contamination from stars in adjacent fibers, while small, will contribute more to the velocity errors for the fainter 2.3-m stars.

6. First data release

6.1. Spatial coverage and global properties

The first RAVE data release presents radial velocities for 24,748 apparently bright stars in the Milky Way. The total number of spectra collected for these stars is 25,274 (including re-observations). Those spectra were obtained during 67 nights between April 11th 2003 and April 2nd 2004, with the exception of one field observed on August 3rd 2004 (second year, but affected by second-order contamination). 12,836 stars in this release are Tycho-2 entries and 11,921 are extracted from the SuperCOSMOS Sky Survey. The stars are distributed over 235 6dF fields (for 240 observed including re-observations) for a total area covered of $\sim 4,760$ sq. deg.

The locations on the sky of the RAVE fields of DR1 are indicated in Fig. 20. This figure presents an Aitoff projection of all RAVE DR1 target fields in Galactic coordinates. Each circle is an RAVE target field (5.7 degrees in diameter). Filled fields are part of this data release. The color coding indicates the number of pointings for a given field (remember that each field contains up to three sets of targets): red for one time, yellow for two and green for three. Among those, 4 fields are re-observed with the same set of targets (3 fields have been re-observed a second time, one field three times). In addition to the normal RAVE target fields, which are restricted to $|b| > 20^\circ$, two fields observed to test the MK-classification scheme in the red RAVE wavelength region are located closer to the Galactic plane.

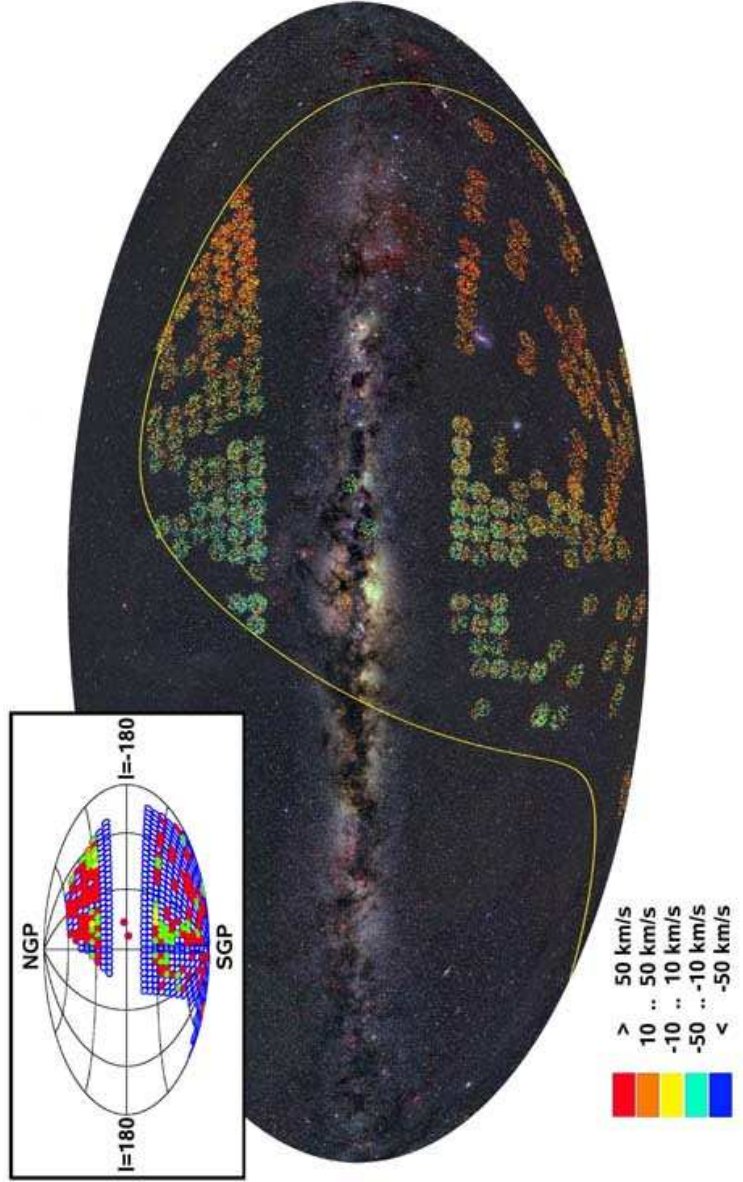


Fig. 20.— Aitoff projection in Galactic coordinates of RAVE first data release fields. With the exception of two test fields, all field centers are located at $|b| \geq 25^\circ$. The heliocentric radial velocity gradient around the sky, traced by the colors, reflects Solar motion and the projection of the different components of velocity down the line-of-sight. The yellow line represents the celestial equator and the background is from Axel Mellinger’s all-sky panorama. The inset shows the location of the RAVE fields for the same projection. Observed fields are color-coded according to the number of times they have been visited; red is for one pointing, yellow two, green three and light brown four.

6.2. Photometry

As noted earlier, the photometry of the input catalog was not homogeneous: the bright part of the sample was selected using a pseudo- I criterion based on Tycho-2 V_T and B_T magnitudes, while the faint part was selected from SuperCOSMOS I data (see section 2.3). To maximize the usability of the DR1 data, cross-identification with optical and near-infrared catalogs (USNO-B, DENIS and 2MASS) is provided. The matches are selected using a nearest-neighbor association. A large search radius is used to check for possible contamination, given that the diameter of a 6dF fiber on the sky is 6.7 arcsec.

In addition to the distance to the nearest neighbor, a quality flag summarizing the reliability of the association is provided in the catalog. This single character flag is set to A for clear association, meaning that the distance between the target and the nearest neighbor is less than 1 arcsec, with no other possible association. The flag value B (or C) is used to warn that two (or more) associations are found within a 1 arcsec radius, and D indicates that the nearest neighbor is further away than 2 arcsec. A value X is given for the flag when no association is found. Table 3 summarizes the outcome of the cross-identification procedure for the various photometric catalogs.

For 2MASS and USNO-B, the cross-identification appears well-defined. The fraction of objects with a flag value different from A is lower than 1%, indicating good agreement between the astrometry in the RAVE input catalog and USNO-B. We therefore expect the level of false identification to be lower than 1% for those catalogs.

The result of the cross-identification with DENIS appears worse than for 2MASS or USNO-B. The main differences are in the categories B and C, where multiple matches are

Table 3. Number and fraction of RAVE targets with a counterpart in the photometric catalogs.

Catalog Name	Number of Objects	% of DR1 with Counterpart	% with quality flag			
			A	B	C	D
2MASS	25,268	99.98%	99.6%	0%	0%	0.4%
DENIS	18,637	73.7%	75.3%	22.3%	1.8%	0.6%
USNO-B	24,814	98.2%	99.2%	0.5%	0%	0.3%

found. This is due to problems in the DENIS catalog where, at the edges of the detector, the astrometry and photometry both become less accurate. In this case, DENIS reports multiple detections of the object for the different scans. Those detections have almost identical magnitudes and positions but could not be associated with the same object. In all those cases, we use the nearest neighbor. As the difference in magnitude is small between the possible matches, this should not affect the overall quality of DENIS associations. Also the reported magnitudes should be of sufficient accuracy for most of the uses of the RAVE catalog. Therefore, even if the cross-identification with the DENIS catalog seems to be poorer according to Table 3, it does not significantly lower the validity of the cross-identification.

The resulting I -band distribution for the RAVE catalog is given in Fig. 21 using the cross-identification with DENIS. This luminosity function exhibits two peaks, defining the bright and faint samples: the first one is centered on $I = 10.2$, the second one on $I = 12$. The shape of this function clearly indicates that, at this point, RAVE does not approximate a random magnitude-limited sample. As discussed earlier in Section 2.3, this is an effect of the input catalog being selected either using the pseudo- I magnitude derived from Tycho-2 photometry or using SuperCOSMOS I in the bright regime, where systematic offsets are to be expected. This effect will be corrected in future RAVE releases with the availability of the full DENIS catalog, which will be used for the input catalog of later data releases.

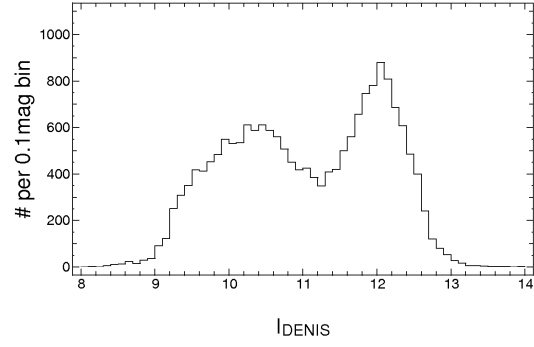


Fig. 21.— DENIS *I* band apparent magnitude distribution of the RAVE DR1 catalog. The two peaks in this distribution are the result of our selection criteria in pseudo-*I* band and delimit the bright and faint samples.

Fig. 22 presents the 2MASS color-color diagram of the data release. Fiducial colors from Table 2 of Wainscoat et al. (1992) have been added for clarity, with dark and light gray curves for dwarf and giant stars respectively. This clearly shows that, as intended, the data released probes both the nearby and more distant Galaxy. As an example, K0 dwarfs in the RAVE catalog span an approximate distance range of ~ 50 pc to ~ 250 pc, while K0 giants are located in the distance range 700 pc to 3 kpc.

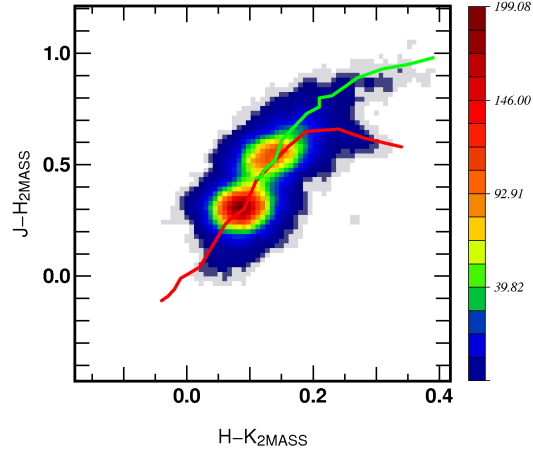


Fig. 22.— 2-MASS infrared color-color diagram for RAVE targets in the first data release. For clarity, the predicted loci for dwarfs and giants (resp. dark and light curves) from Wainscoat et al. (1992) have been added. Again the color-code indicates the number of objects per bin.

6.3. Proper motions

The input catalog for the DR1 has been built upon Tycho-2 and SSS, and both of these provide proper motions. When available, we also used proper motions from the Starnet 2.0 catalog which is presently being compiled at the Astronomisches Rechen-Institut, Heidelberg. It is based on the Starnet catalog of positions and proper motions (Röser 1996) of 4.3 million stars based on measurements from the Astrographic Catalog and GSC 1.2 (Morrison et al. 2001). The average rms error of proper motions in Starnet is 5 mas/yr, being mainly influenced by the accuracy of GSC 1.2. During the last decade new, highly accurate, astrometric catalogs became available, namely Tycho-2, UCAC2 and, for fainter stars, 2MASS. Starnet 2.0 combines Starnet with these three catalogs in a rigorous, weighted least-squares adjustment to derive mean positions and proper motions. Weights for the individual positions in the catalogs have been attributed according to the accuracy of the position measurements in the sources: for the Astrographic Catalogs weights were taken from Röser & Høg (1993), for GSC 1.2 from Morrison et al. (2001), for Tycho-2 from Høg et al. (2000), for UCAC2 from Zacharias et al. (2004) and for 2MASS from Cutri et al. (2003). The mean errors of the proper motions given in Starnet 2.0 are calculated from the individual weights. They are not calculated from the dispersion of the residuals due to the low degree of freedom in each individual adjustment. The average mean error in the proper motions of Starnet 2.0 stars in this catalog is 2.6 mas/yr in each coordinate.

Neither Starnet nor Tycho-2 or UCAC2 are complete with regard to stars with proper motions in the range between approximately 30 mas/yr and 150 mas/yr. This is mainly due to the fact that the epoch difference between the Astrographic Catalog and modern catalogs is almost 100 years. Therefore, the identifications of these moderately high proper motion stars is uncertain. To overcome this difficulty for Starnet 2.0, an auxiliary catalog has been constructed from the difference between 2MASS and GSC 1.2, with an epoch difference of about 20 years. The average mean error in the proper motions of the stars from this source is 18 mas/yr. Proper motions are taken from this auxiliary catalog whenever no other proper motions could be found. A summary of the contribution of each proper motion source to DR1 is given in Table 4. The source of the proper motion is also flagged in the catalog (see Appendix A).

6.4. Data product and data access

Due to the size of the catalog, RAVE DR1 is only accessible online. The catalog fields are nevertheless described in Appendix A, Tables 5 to 7. The catalog can be retrieved or

queried from the RAVE collaboration website.¹¹

As the catalog is large, and will grow in size as further releases are made public, query tools are provided on those websites. Users can access the catalog using different techniques, either with a standard query interface or by field, using their position on the sky (this access mode is provided via a clickable map). For DR1 only tabular data are provided and VOTable¹² formatted outputs are offered for ease of use with the Virtual Observatory tools. For the subsequent releases, spectra will be made available, requiring the inclusion of more VO formats (enabling a proper description of a spectrum).

In the field query mode, links to the Aladin Sky Atlas (Bonnarel et al. 2000) are generated, providing additional information in addition to VO tools to exploit the data. However, this link to Aladin is not provided for the standard catalog query, as the area on the sky is not restricted. The first data release catalog, as well as subsequent releases, will also be electronically available at the CDS in the VizieR database (Ochsenbein et al. 2000).

Again, DR1 includes from the RAVE survey only radial velocities and associated errors, described in detail above. Cross-matching with standard astrometric and photometric catalogs are provided for ease of use. Stellar parameters are not part of this release, as the first year spectra are contaminated by second order light, which means that very detailed analysis is required to extract meaningful values.

7. Conclusions

This first data release presents radial velocities for 24,748 individual stars in the range $9 \lesssim I_{DENIS} \lesssim 12.5$, obtained from spectra in the infrared Calcium-triplet region at a median resolution of 7,500. The total sky coverage of this catalog is $\sim 4,760$ square degrees. We demonstrated that the radial velocities are not affected by any trend in color or SNR using both external data and RAVE repeat observations. The resulting variance for each set of validation data is consistent with our estimated errors.

DR1 does not include information about chemical abundances and other atmospheric parameters, for reasons described above. The quality of the currently acquired spectra is good enough for derivation of T_{eff} , gravity, $[M/H]$, $[\alpha/Fe]$, $V_{\text{rot}} \sin i$, and micro-turbulence (Fiorucci & Munari 2006), and we expect to include chemical and atmospheric data in

¹¹<http://www.rave-survey.org>.

¹²VOTable is the standard format for tabular data in the Virtual Observatory.

subsequent data releases.

RAVE is planned to observe until 2010 and will acquire up to 1,000,000 spectra. Incremental releases, containing radial velocities, stellar parameters as well as spectra, are now planned on an approximately yearly basis, providing an unprecedented sample of stellar kinematics and chemical abundances in the range of magnitudes probing scales between the very local (Hipparcos based) radial velocity surveys (GCS and Famaye et al. 2005) and the more distant SDSSII/SEGUE and surveys with AAOmega, therefore completing our picture of the Milky Way.

Acknowledgments

We are indebted to the referee Sydney van den Bergh, whose timely and justified comments helped us improve the clarity of the manuscript.

MS, AS, CB acknowledge financial support from the German Research Foundation (DFG).

MS acknowledges financial support from the David and Lucile Packard Foundation.

TZ acknowledges financial support from the Slovenian Research Agency.

AS is supported by the Alexander von Humboldt Foundation.

KCF, QAP, RC, JB-H, BKG, MW are supported from an Australian Research Council Grant for the RAVE project.

GMS is funded by a Particle Physics and Astronomy Research Council PhD Studentship.

RFGW acknowledges seed money from the School of Arts and Sciences at JHU, plus NSF grant AST-0508996.

OB acknowledges financial support from the CNRS/INSU/PNG.

EKG is supported by the Swiss National Science Foundation under the grants 200021-101924 and 200020-106260.

AH and MCS acknowledge financial support from NOVA and the Netherlands Organisation for Scientific Research (NWO)

JFN and JP's participation in RAVE are supported by Canada's NSERC through a Special Research Opportunities grant

HE and MS acknowledge support by the Federal Ministry for Education and Research (BMBF) under FKZ 05AE2EE1/4 and 01AK804A.

JF acknowledges support through grants from the W.M. Keck Foundation and the Gordon and Betty Moore Foundation, to establish a program in data-intensive science at JHU.

The role of the Anglo-Australian Observatory in providing resources for the first nine months of observation is gratefully acknowledged.

This research has made use of the VizieR catalog access tool, CDS, Strasbourg, France. Data verification is partially based on observations taken at the Observatoire de Haute Provence (OHP) (France), operated by the French CNRS.

REFERENCES

- Abadi, M. G., Navarro, J. F., Steinmetz, M., & Eke, V. R. 2003, *ApJ*, 597, 21
- Abadi, M. G., Navarro, J. F., & Steinmetz, M. 2006, *MNRAS*, 365, 47
- Baranne, A., Queloz, D., Mayor, M., Adrianzyk, G., Knispel, G., Kohler, D., Lacroix, D., Meunier, J.-P., Rimbaud, G., & Vin, A. 1996, *A&AS*, 119, 373
- Bessell, M. S., 1979, *PASP*, 91, 589
- Bessell, M. S., 1986, *PASP*, 98, 1303
- Bessell, M. S., 2000, *PASP*, 112, 961
- Belokurov, V. et al. 2006, *ApJL*, in press
- Blair, M., & Gilmore, G. 1982, *PASP*, 94, 742
- Bonnarel, F., Fernique, P., Bienayme, O., Egret, D., Genova, F., Louys, M., Ochsenbein, F., Wenger, M., & Bartlett, J. G. 2000, *A&AS*, 143, 33
- Brook, C., Gibson, B., Martel, H. & Kawata, D. 2005, *ApJ*, 630, 298
- Bullock, J. S., & Johnston, K. V. 2005, *ApJ*, 635, 931
- Colless, M., Dalton, G., Maddox, S., Sutherland, W., Norberg, P., Cole, S., Bland-Hawthorn, J., Bridges, T., Cannon, R., Collins, C., Couch, W., Cross, N., Deeley, K., De Propriis, R., Driver, S. P., Efsthathiou, G., Ellis, R. S., Frenk, C. S., Glazebrook, K., Jackson, C., Lahav, O., Lewis, I., Lumsden, S., Madgwick, D., Peacock, J. A., Peterson, B. A., Price, I., Seaborne, M., & Taylor, K. 2001, *MNRAS*, 328, 1039
- Cutri, R. M., Skrutskie, M. F., van Dyk, S., Beichman, C. A., Carpenter, J. M., Chester, T., Cambresy, L., Evans, T., Fowler, J., Gizis, J., Howard, E., Huchra, J., Jarrett, T., Kopan, E. L., Kirkpatrick, J. D., Light, R. M., Marsh, K. A., McCallon, H., Schneider, S., Stiening, R., Sykes, M., Weinberg, M., Wheaton, W. A., Wheelock, S., & Zacarias, N. 2003, *The 2MASS All-Sky Catalog of Point Sources*, University of Massachusetts and Infrared Processing and Analysis Center, (IPAC/California Institute of Technology)
- de Simone, R., Wu, X., Tremaine, S. 2004, *MNRAS*, 350, 627
- Dehnen, W. 2000, *AJ*, 119, 800

- Eggen, O. J., Lynden-Bell, D., & Sandage, A. R. 1962, *ApJ*, 136, 748
- Epchtein, N., Deul, E., Derriere, S., Borsenberger, J., Egret, D., Simon, G., Alard, C., Balázs, L. G., de Batz, B., Cioni, M.-R., Copet, E., Dennefeld, M., Forveille, T., Fouqué, P., Garzón, F., Habing, H. J., Holl, A., Hron, J., Kimeswenger, S., Lacombe, F., Le Bertre, T., Loup, C., Mamon, G. A., Omont, A., Paturel, G., Persi, P., Robin, A. C., Rouan, D., Tiphène, D., Vauglin, I., & Wagner, S. J. 1999, *A&A*, 349, 236
- ESA 1997, The Hipparcos and Tycho catalogues. Astrometric and photometric star catalogues derived from the ESA Hipparcos Space Astrometry Mission, Publisher: Noordwijk, Netherlands: ESA Publications Division, 1997, Series: ESA SP Series vol no: 1200
- Famaey, B., Jorissen, A., Luri, X., Mayor, M., Udry, S., Dejonghe, H., & Turon, C., *A&A*, 430, 165
- Fiorucci, M., Munari, U., & the RAVE collaboration 2005, *AAS*, 207, 123.07
- Freeman, K. C., & Bland-Hawthorn, J. 2002, *ARA&A*, 40, 487
- Gilmore, G., Wyse, R. F. G., & Jones, J. B. 1995, *AJ*, 109, 1095
- Gilmore, G., Wyse, R. F. G., & Norris, J. E. 2002, *ApJ*, 574, 39
- Governato, F. et al, 2004, *ApJ*, 607, 688
- Hambly, N. C., Mc Gillivray, H. T., Read, M. A., Tritton, S. B., Thomson, E. B., Kelly, B. D., Morgan, D. H., Smith, R. E., Driver, S. P., Williamson, J., Parker, Q. A., Hawkins, M. R. S., Williams, P. M., & Lawrence, A. 2001, *MNRAS*, 326, 1279
- Hambly, N. C., Irwin, M. J., & Mc Gillivray, H. T. 2001, *MNRAS*, 326, 1295
- Hambly, N. C., Davenhall, A. C., Irwin, M. J., & Mc Gillivray H. T. 2001, *MNRAS*, 326, 1315
- Hartley, M., & Dawe, J. A. 1981, *PASA*, 4, 251
- Helmi, A., Navarro, J. F., Nordström, B., Holmberg, J., Abadi, M. G., & Steinmetz, M. 2006, *MNRAS*, 365, 1309
- Høg, E., Fabricius, C., Makarov, V. V., Urban, S., Corbin, T., Wycoff, G., Bastian, U., Schwekendiek, P., & Wicenec, A. 2000, *A&A*, 355, L27
- Ibata, R. A., Gilmore, G., & Irwin, M. J. 1994, *Nature*, 370, 194

- Ibata, R., Irwin, M., Lewis, G., Ferguson, A. M. N., & Tanvir, N. 2001, *Nature*, 412, 49
- Jones, D. H., Saunders, W., Colless, M., Read, M. A., Parker, Q. A., Watson, F. G., Campbell, L. A., Burkey, D., Mauch, T., Moore, L., Hartley, M., Cass, P., James, D., Russell, K., Fiegert, K., Dawe, J., Huchra, J., Jarrett, T., Lahav, O., Lucey, J., Mamon, G. A., Proust, D., Sadler, E. M., & Wakamatsu, K. 2004, *MNRAS*, 355, 747
- Katz, D. et al. 2004, *MNRAS* 354, 1223
- Kuijken, K., & Gilmore, G. 1989a, *MNRAS*, 239, 571
- Kuijken, K., & Gilmore, G. 1989b, *MNRAS*, 239, 605
- Kuijken, K., & Gilmore, G. 1989c, *MNRAS*, 239, 651
- Kurtz, M. J., Mink, D. J., Wyatt, W. F., Fabricant, D. G., Torres, G., Kriss, G. A., & Tonry, J. L. 1992, *ASPC*, 25, 432
- Lewis, I. J., Cannon, R. D., Taylor, K., Glazebrook, K., Bailey, J. A., Baldry, I. K., Barton, J. R., Bridges, T. J., Dalton, G. B., Farrell, T. J., Gray, P. M., Lankshear, A., McCowage, C., Parry, I. R., Sharples, R. M., Shortridge, K., Smith, G. A., Stevenson, J., Straede, J. O., Waller, L. G., Whittard, J. D., Wilcox, J. K., & Willis, K. C. 2002, *MNRAS*, 333, 279
- Meza, A., Navarro, J. F., Abadi, M. G., & Steinmetz, M. 2005, *MNRAS*, 359, 93
- Miszalski, B. 2006, *MNRAS*, submitted
- Monet, D. G., Levine, S. E., Canzian, B., Ables, H. D., Bird, A. R., Dahn, C. C., Guetter, H. H., Harris, H. C., Henden, A. A., Leggett, S. K., Levison, H. F., Luginbuhl, C. B., Martini, J., Monet, A. K. B., Munn, J. A., Pier, J. R., Rhodes, A. R., Rieke, B., Sell, S., Stone, R. C., Vrba, F. J., Walker, R. L., Westerhout, G., Brucato, R. J., Reid, I. N., Schoening, W., Hartley, M., Read, M. A., & Tritton, S. B. 2003, *AJ*, 125, 984
- Morrison, J. E., Röser, S., McLean, B., Bucciarelli, B., & Lasker, B. 2001, *AJ* 121, 1752
- Munari, U., Agnolin, P., Tomasella, A. 2001, *BaltA*, 10, 613
- Munari, U. 2003, ed. *Gaia Spectroscopy, Science and Technology*, ASP Conf. Ser. 298
- Munari, U., Sordo, R., Castelli, F., & Zwitter, T. 2005, *A&A*, 442, 615
- Navarro, J. F., Helmi, A., & Freeman, K. C. 2004, *ApJ*, 601, 43

- Newberg, H. J. 2003, & Sloan Digital Sky Survey Collaboration 2003, AAS, 203, 112.11
- Nordström, B., Mayor, M., Andersen, J., Holmberg, J., Pont, F., Jørgensen, B. R., Olsen, E. H., Udry, S., & Mowlavi, N. 2004, A&A, 418, 989
- Ochsenbein, F., Bauer, P., & Marcout, J. 2000 A&AS, 143,230
- Odenkirchen, M., Grebel, E. K., Rockosi, C. M., Dehen, W., Ibata, R., Rix, H.-W., Stolte, A., Wolf, C., Anderson, J. E., Bahcall, N. A., Brinkmann, J., Csabai, I., Hennessy, G., Hindsley, R. B., Ivezić, Z., Lupton, R. H., Munn, J. A., Pier, J. R., Stoughton, C., & York, D. G. 2001, ApJ, 548, 165
- Parker, Q. A., & Watson, F. G. 1990, A&AS, 84, 455
- Piquard, S., Halbwachs, J.-L., Fabricius, C., Geckeler, R., Soubiran, C., & Wicenec, A. 2001, A&A, 373, 576
- Pont, F., Zinn, R., Gallart, C., Hardy, E., & Winnick, R. 2004, AJ, 127, 840
- Quillen, A.C., Minchev, I. 2005, AJ, 130, 576
- Robertson, B., Bullock, J. S., Font, A.S., Johnston, K. V. & Hernquist, L., 2005, ApJ, 632, 872
- Rodgers, A.W., Conroy, P., & Bloxham, G. 1988, PASP, 100, 626
- Röser, S., & Høg, E. 1993 TYCHO Reference Catalogue (TRC) Workshop on Databases for Galactic Structure (1993) A. G. D. Philip, B. Hauck and A. R. Upgren (Eds.) , L. Davis Press, 1993, p.137
- Röser, S. 1996, IAU Symp. 172, p. 481
- Samus, N. N., Durlevich, O. V., et al. 2004, Combined General Catalog of Variable Stars (GCVS4.2), Institute of Astronomy of Russian Academy of Sciences and Sternberg State Astronomical Institute of the Moscow State University, <http://vizier.u-strasbg.fr/viz-bin/Cat?II/250>
- Seabroke, G. M. 1879, MNRAS, 39,450
- Seabroke, G. M. 1887, MNRAS, 47,93
- Seabroke, G. M. 1889, MNRAS, 50,72
- Sommer-Larsen, J., Gotz, M. & Portinari, L. 2003, ApJ, 596, 47

- Steinmetz, M., & Navarro, J. F. 2002, *New A*, 7, 155
- Steinmetz, M. 2003, *ASP Conf. Ser.*, 298, 381
- Tolstoy, E., Venn, K.A., Shetrone, M., Primas, F., Hill, V., Kauefr, A & Szeifert, T. 2003, *AJ*, 125, 707
- Tonry, J., & Davis, M. 1979, *AJ*, 84, 1511
- Unavane, M., Wyse, R.F.G. & Gilmore, G. 1996, *MNRAS*, 278, 727
- Vogel, H. C. 1873, *Astron. Nach.*, 82, 291
- Wainscoat, R. J., Cohen, M., Volk, K., Walker, H. J., & Schwartz, D. E. 1992, *ApJS*, 83, 111
- Watson, F. G., Parker, Q. A., Bogatu, G., Farrell, T. J., Hingley, B. E., & Miziarski, S. 2000, *SPIE*, 408, 123
- Wilkinson, M. et al. 2005, *MNRAS*, 359, 1306
- Wyse, R.F.G. & Gilmore, G. 2006, in ‘Resolved Stellar Populations’ eds D. Valls-Gabaud and M. Chavez, *ASP Conference proceedings*, in press (astro-ph/0510025)
- Wyse, R. F. G., & Gilmore, G. 1992, *MNRAS*, 257, 1
- Wyse, R. F. G., & Gilmore, G. 1995, *AJ*, 110, 2771
- Yanny, B., Newberg, H. J., Grebel, E. K., Kent, S., Odenkirchen, M., Rockosi, C. M., Schlegel, D., Subbarao, M., Brinkmann, J., Fukugita, M., Ivezić, Z., Lamb, D. Q., Schneider, D. P., & York, D. G. 2003, *ApJ*, 588, 824
- Zacharias, N., Urban, S. E., Zacharias, M. I., Wycoff, G. L., Hall, D. M., Monet, D. G., & Rafferty, T. J. 2004, *AJ*, 127, 3043
- Zwitter, T. 2002, *A&A*, 386, 748
- Zwitter, T., & Munari, U. 2004, in *Environments and evolution of double and multiple stars*, IAU Coll. 191, C. Scarfe (ed.), *RevMexAA*, 21, 251
- Zwitter, T., Castelli, F., & Munari, U. 2004, *A&A*, 417, 1055

Appendix A. Catalog description

This appendix presents the different columns that are provided in the first data release.

Table 4. Summary of the proper motion sources.

SPM Flag	Catalog Name	Number of sources	% of DR1
0	No proper motion	13	0.05
1	Tycho-2	218	0.86
2	SSS	7,396	29.3
3	STARNET 2.0	17,465	69.1
4	2MASS+GSC 1.2	182	0.72

Table 5. Description of the RAVE catalog.

Field Number	Name	Unit	NULL value	Description
1	OBJECTID	-	-	Internal identifier
2	RA	deg	-	Right ascension (J2000)
3	DE	deg	-	Declination (J2000)
4	Glon	deg	-	Galactic longitude
5	Glat	deg	-	Galactic latitude
6	RV	km/s	-	Radial Velocity
7	eRV	km/s	-	Internal radial velocity error
8	pmRA	mas/yr	9999.9	Proper motion RA
9	epmRA	mas/yr	9999.9	Proper motion error RA
10	pmDE	mas/yr	9999.9	Proper motion DE
11	epmDE	mas/yr	9999.9	Proper motion error DE
12	Spm	-	-	Source proper motion (see Section 6.3)
13	Imag	mag	-	Input catalog <i>I</i> magnitude
14	Obsdate	yyyymmdd	-	Date of observation
15	FieldName	-	-	RAVE observations field
16	FiberNumber	-	-	Fiber number on plate
17	CorrelationCoeff	-	-	Tonry-Davis correlation coefficient <i>R</i>
18	PeakHeight	-	-	Height of the correlation function peak
19	PeakWidth	km/s	-	Width of the correlation function peak width
20	CorrectionRV	km/s	-	Radial Velocity correction applied
21	SkyRV	km/s	-	Sky radial velocity in fiber

Table 5—Continued

Field Number	Name	Unit	NULL value	Description
22	SkyeRV	km/s	-	Sky radial velocity error
23	SkyCorrelation	-	-	Tonry-Davis correlation coefficient for sky spectra
24	PlateNumber	-	-	Physical plate number
25	SNRatio	-	-	Signal to Noise ratio
26	BT	mag	99.99	B_T magnitude from Tycho-2
27	eBT	mag	99.99	B_T magnitude error from Tycho-2
28	VT	mag	99.99	V_T magnitude from Tycho-2
29	eVT	mag	99.99	V_T magnitude error from Tycho-2
30	USNOID	-	XXX	USNO-B identifier
31	DisUSNO	mas	99.999	Distance to USNO source
32	B1	mag	99.99	USNO-B $B1$ magnitude
33	R1	mag	99.99	USNO-B $R1$ magnitude
34	B2	mag	99.99	USNO-B $B2$ magnitude
35	R2	mag	99.99	USNO-B $R2$ magnitude
36	IUSNO	mag	99.99	USNO-B I magnitude
37	XidQualityFLAGUSNO	-	X	Cross-identification quality FLAG USNO-B (see table 6)
38	DENISID	-	XXX	DENIS identifier
39	DisDENIS	mas	99.999	Distance to DENIS source
40	IDENIS	mag	99.999	DENIS I magnitude
41	eIDENIS	mag	99.999	DENIS I magnitude error
42	JDENIS	mag	99.999	DENIS J magnitude
43	eJDENIS	mag	99.999	DENIS J magnitude error

Table 5—Continued

Field Number	Name	Unit	NULL value	Description
44	KDENIS	mag	99.999	DENIS K magnitude
45	eKDENIS	mag	99.999	DENIS K magnitude error
46	XidQualityFLAGDENIS	-	X	Cross-identification quality FLAG DENIS (see Table 6)
47	TWOMASSID	-	XXX	2MASS identifier
48	Dis2MASS	mas	99.999	Distance to 2MASS source
49	J2MASS	mag	99.999	2MASS J magnitude
50	eJ2MASS	mag	99.999	2MASS J magnitude error
51	H2MASS	mag	99.999	2MASS H magnitude
52	eH2MASS	mag	99.999	2MASS H magnitude error
53	K2MASS	mag	99.999	2MASS K magnitude
54	eK2MASS	mag	99.999	2MASS K magnitude error
55	TWOMASSphotFLAG	-	XXX	2MASS photometry flag
56	XidQualityFLAG2MASS	-	X	Cross-identification quality flag 2-MASS (see Table 6)
57	ZeroPointQualityFLAG	-	-	zero-point quality flag (see Table 1)
58	VarFLAG	-	-	Variability flag, '*' if in GCVS2.0
59	SpectraQualityFLAG	-	-	Spectra quality flag (see Table 7)

Appendix B. External data

This appendix presents the calibration measurements obtained for the RAVE survey during the first year of operation. Those calibration data are divided in three tables, according to their source (instrument or catalog). A complete description of those data is given in Section 5.6.

Table 6. Summary of the cross-identification flag.

Flag value	Description
A	1 association within 1 arcsec.
B	2 associations within 1 arcsec.
C	More than 2 associations within 1 arcsec.
D	Nearest neighbor more than 2 arcsec. away.
X	No association found.

Table 7. Spectra quality flag summary table. The values can be combined to give a more accurate description of the spectra.

Flag value	Description
a	Asymmetric Ca lines
c	Cosmic ray resulting in asymmetric correlation function
e	Emission line spectra
n	Noise dominated spectra, broad correlation function
l	No lines visible, either strong noise or misplaced fiber
w	Weak lines, radial velocity can be unreliable
g	Strong ghost affecting the wavelength interval used for radial velocity calculation.
t	Bad template fit
s	Strong residual sky emission
cc	Bad continuum
r	Red part of the spectra shows problems, noisy
b	Blue part of the spectra shows problems, noisy
p	Possible binary/double lined

Table 8. List of RAVE targets observed with the ELODIE spectrograph. This table presents the RAVE observations as well as the ELODIE measurements. DENIS and 2MASS photometry are also reported. The radial velocity error for RAVE measurements correspond to the internal error and are not corrected for zero-point accuracy. Objects flagged with (*) are binary stars and are discarded from the analysis. The V_T/I column contains the Tycho-2 V_T magnitudes for Tycho-2 objects and SSS I magnitude for other targets.

Identifier	RAVE		ELODIE		Rad. Vel. diff. (km/s)	V_T/I (mag)	I_{DENIS} (mag)	$J-H$ (mag)	$H-K$ (mag)
	Rad. Vel.	Rad. Vel.	Rad. Vel.	Rad. Vel.					
	(km/s)	error (km/s)	(km/s)	error (km/s)					
T5027_00352_1	-7.9	2.2	-8.9	1.0	1.0	10.43	9.03	0.57	0.16
T5027_00578_1	-32.0	1.5	-32.3	1.0	0.3	10.58	9.55	0.34	0.14
T5027_00389_1	39.9	2.0	39.0	1.0	0.9	11.18	9.74	0.68	0.17
T5027_00374_1	-47.5	1.7	-43.7	1.0	0.2	11.42	10.14	0.66	0.17
T5031_00478_1(*)	-22.4	2.3	-42.4	1.0	20.0	11.26	...	0.31	0.10
C1430054-094720	92.7	2.1	91.9	1.0	-0.2	11.47	11.85	0.62	0.11
C1429286-091608	-19.2	1.2	-19.2	1.0	0.0	10.06	10.49	0.55	0.12

Table 9. 2.3m observations of RAVE targets. This table list the RAVE targets observed with the 2.3 m long-slit spectrograph in Siding Spring. RAVE measurements, as well as DENIS I magnitude, radial velocity difference and 2MASS colors are also reported. Stars marked with (*) are variable or binary objects and are discarded from the analysis. The estimated radial velocity error for all 2.3 m data is 1.5 km/s.

Identifier	RAVE		2.3 m		R value 2.3 m	V_T/I (mag)	I_{DENIS} (mag)	$J-H$ (mag)	$H-K$ (mag)
	Rad. Vel. (km/s)	Rad. Vel. error (km/s)	Rad. Vel. (km/s)	Rad. Vel. diff. (km/s)					
C1032220-225303	103.2	2.4	103.6	-0.4	43.4	11.82	12.43	0.30	0.01
C1032220-225303	103.8	3.4	103.6	0.2	43.4	11.82	12.43	0.30	0.01
C1032264-241144	52.4	2.1	54.3	-1.9	75.9	11.85	12.20	0.32	0.08
C1032264-241144	47.9	1.5	54.3	-6.4	75.9	11.85	12.20	0.32	0.08
C1033394-215304	118.8	2.7	120.4	-1.6	78.2	11.96	12.31	0.50	0.09
C1033426-214025(*)	63.2	1.8	5.3	57.9	90.4	11.53	12.33	0.26	0.07
C1033426-214025(*)	48.2	2.3	5.3	42.9	90.4	11.53	12.33	0.26	0.07
C1033528-220832	34.3	2.3	25.2	9.1	74.8	11.99	12.33	0.22	0.10
T6073_00197_1	40.7	2.1	38.1	2.6	124.2	11.53	9.77	0.72	0.20
T6073_00197_1	40.0	0.6	38.1	1.9	124.2	11.53	9.77	0.72	0.20
T6074_00342_1	-30.3	2.1	-22.5	-7.8	106.8	11.35	9.37	0.44	0.11
T6074_00342_1	-16.6	1.1	-22.5	5.9	106.8	11.35	9.37	0.44	0.11
T6620_00749_1(*)	-24.4	1.9	13.6	-38.0	75.2	11.77	11.10	0.26	0.09
T6620_00749_1(*)	-22.4	0.9	13.6	-36.0	75.2	11.77	11.10	0.26	0.09
T6620_00941_1	86.7	2.4	87.8	-1.1	132.7	11.35	10.18	0.52	0.11
T6624_00025_1	38.3	4.3	45.4	-7.1	101.7	10.71	9.80	0.52	0.17
T6624_00025_1	38.6	0.5	45.4	-6.8	101.7	10.71	9.80	0.52	0.17
T6624_01181_1	22.7	1.8	24.2	-1.5	90.3	10.89	10.35	0.19	0.09

Table 9—Continued

Identifier	RAVE		2.3 m		R value 2.3 m	V_T/I (mag)	I_{DENIS} (mag)	$J-H$ (mag)	$H-K$ (mag)
	Rad. Vel. (km/s)	Rad. Vel. error (km/s)	Rad. Vel. (km/s)	Rad. Vel. diff. (km/s)					
T6624_01181_1	23.2	0.7	24.2	-1.0	90.3	10.89	10.35	0.19	0.09
T6637_00126_1	27.6	2.0	31.6	-4.0	101.8	10.55	10.67	0.38	0.07
T6637_00126_1	26.8	0.8	31.7	-4.8	101.8	10.55	10.67	0.38	0.07
C1025107-255418	317.1	1.7	315.2	1.9	116.4	11.58	11.54	0.54	0.09
C1025107-255418	317.2	1.0	315.2	2.0	116.4	11.58	11.54	0.54	0.09
C1025310-260312(*)	27.0	1.7	-1.8	28.8	105.2	11.89	11.91	0.32	0.07
C1025310-260312(*)	1.3	2.1	-1.8	3.1	105.2	11.89	11.91	0.32	0.07
C1026269-255018	18.6	2.6	15.6	3.0	65.3	11.82	11.88	0.30	0.08
C1026269-255018	16.5	1.8	15.6	0.9	65.3	11.82	11.88	0.30	0.08
T6623_00942_1	16.7	1.8	13.2	3.5	93.4	10.06	9.42	0.36	0.15
T6623_00942_1	13.9	0.9	13.2	0.7	93.4	10.06	9.42	0.36	0.15
T6627_01266_1(*)	-3.0	2.6	36.2	-39.2	78.9	10.87	10.26	0.17	0.11
T9317_01217_1	7.0	2.0	11.1	-4.1	78.6	10.71	9.91	0.22	0.06
T9459_00225_1	-6.0	1.1	-7.2	1.2	103.4	10.66	10.16	0.27	0.06
T9459_00391_1	5.5	1.8	7.2	-1.7	73.3	11.22	10.10	0.63	0.09
T9459_00433_1(*)	-17.9	2.3	-30.7	12.8	53.0	10.24	9.93	0.16	0.02
T9459_00433_1(*)	-22.0	2.1	-30.7	8.7	53.0	10.24	9.93	0.16	0.02
T9459_01509_1	45.0	1.6	45.1	-0.1	72.5	11.84	10.45	0.62	0.13
T9462_00133_1	-3.7	1.9	-4.5	0.8	76.5	11.34	10.30	0.43	0.15

Table 9—Continued

Identifier	RAVE		2.3 m		R value 2.3 m	V_T/I (mag)	I_{DENIS} (mag)	$J-H$ (mag)	$H-K$ (mag)
	Rad. Vel.	Rad. Vel.	Rad. Vel.	Rad. Vel.					
	(km/s)	error (km/s)	(km/s)	diff. (km/s)					
T9462_01174_1	-17.4	1.5	-16.4	-1.0	123.1	11.86	10.14	0.61	0.24
T9463_00658_1	46.7	1.1	43.9	2.8	91.1	10.76	...	0.30	0.10
T9463_01298_1	35.6	1.9	36.3	-0.7	75.6	11.42	10.50	0.37	0.05
T9467_00768_1	71.8	1.6	74.5	-2.7	111.4	11.57	9.79	0.71	0.21
T9318_00046_1	-0.5	1.3	1.1	-1.6	81.3	11.80	...	0.60	0.09
T9318_00362_1	15.1	1.6	15.8	-0.7	92.3	10.64	...	0.17	0.09
T9319_00355_1	2.0	1.7	3.5	-1.5	96.9	10.74	9.63	0.47	0.12
T9458_01749_1	38.2	1.0	38.3	-0.1	117.1	11.52	...	0.75	0.20
T9458_02394_1	114.4	1.6	116.8	-2.4	106.3	11.61	10.23	0.73	0.11
T9459_00973_1	85.4	1.3	86.4	-1.0	94.1	10.62	9.68	0.53	0.06
T9459_01430_1	-3.7	1.4	-1.0	-2.7	95.5	10.94	10.23	0.27	0.06
T9459_01430_1	-3.2	1.8	-1.0	-2.1	95.5	10.94	10.23	0.27	0.06
T9459_01822_1	24.1	1.6	27.0	-2.9	91.9	11.19	9.85	0.62	0.15
T9460_00265_1	-0.8	1.7	0.0	-0.8	92.5	12.17	10.57	0.56	0.14
T9460_00353_1	-45.4	1.4	-42.2	-3.2	85.9	11.11	9.57	0.75	0.20
T9462_00226_1	-23.3	3.0	-25.3	2.0	68.4	11.35	10.74	0.26	0.08
T9462_02202_1	27.3	1.5	23.7	3.6	102.2	10.35	9.85	0.29	0.06
T9463_01633_1	16.0	3.8	16.4	-0.4	74.2	12.33	11.47	0.39	0.04
T9464_00658_1	1.3	1.0	-0.7	2.0	80.7	10.82	10.09	0.22	0.07

Table 9—Continued

Identifier	RAVE		2.3 m		R value 2.3 m	V_T/I (mag)	I_{DENIS} (mag)	$J-H$ (mag)	$H-K$ (mag)
	Rad. Vel.	Rad. Vel.	Rad. Vel.	Rad. Vel.					
	(km/s)	error (km/s)	(km/s)	diff. (km/s)					
T9464_00658_1	0.4	1.5	-0.7	1.1	80.7	10.82	10.09	0.22	0.07
T9464_00865_1	8.3	1.5	3.2	5.1	67.2	10.76	9.96	0.33	0.15
T9467_00478_1	23.1	6.6	22.4	0.7	98.9	11.80	10.24	0.67	0.22
T9317_01143_1	13.5	2.8	19.7	-6.2	100.6	11.69	10.48	0.55	0.14
T9317_01143_1	17.5	1.6	19.7	-2.2	100.6	11.69	10.48	0.55	0.14
T9458_00843_1	9.7	1.2	8.6	1.1	87.8	10.27	9.50	0.35	0.11
T9458_00934_1	-41.9	1.3	-41.0	-0.9	112.2	12.10	10.97	0.59	0.11
T9460_01761_1	31.1	1.1	34.6	-3.5	80.0	11.03	10.34	0.22	0.09
T9462_01690_1	0.3	2.7	2.2	-1.9	111.6	11.35	9.83	0.58	0.16
T9317_00415_1	22.3	2.4	20.3	2.0	116.1	11.43	10.34	0.48	0.13
T9458_02020_1	23.2	1.9	17.0	6.2	58.5	9.49	9.28	-0.04	0.12
T9460_00219_1	75.3	1.2	75.2	0.1	157.2	11.71	10.17	0.59	0.16
T9462_01219_1(*)	57.5	10.4	30.4	27.1	88.9	9.91	9.54	0.10	0.08
T9464_00050_1	28.9	0.9	25.6	3.3	100.4	10.69	10.15	0.20	0.06
C1519196-191359	-407.3	2.3	-409.0	1.7	76.8	11.32	12.12	0.66	0.14
C1508217-085010	-289.8	3.0	-287.8	-2.0	72.7	11.29	11.91	0.49	0.07
C1536201-144228	-329.2	2.8	-330.4	1.2	46.4	11.82	12.42	0.49	0.16
T7274_00734_1	407.9	1.5	407.8	0.1	108.2	10.06	...	0.46	0.07
C1905210-751503	-153.1	3.6	-148.9	-4.2	79.6	11.69	12.00	0.64	0.14

|
∞
|

Table 9—Continued

Identifier	RAVE		2.3 m		R value 2.3 m	V_T/I (mag)	I_{DENIS} (mag)	$J-H$ (mag)	$H-K$ (mag)
	Rad. Vel. (km/s)	Rad. Vel. error (km/s)	Rad. Vel. (km/s)	Rad. Vel. diff. (km/s)					
T8395_01513_1	-296.3	2.0	-295.2	-1.1	140.4	11.30	9.99	0.51	0.05
T6671_00389_1	0.7	2.0	-5.0	5.7	79.0	10.80	10.14	0.26	0.10
C1435432-164545	-15.1	3.7	-17.2	2.1	40.4	11.51	12.16	0.57	0.10
C1254296-164722	71.7	2.2	74.3	-2.6	44.0	10.82	...	0.38	0.08
C1532041-135910	44.2	1.4	36.8	7.4	43.5	11.81	12.09	0.45	0.09
C2030129-660620	91.6	2.3	91.9	-0.3	63.6	11.54	12.09	0.37	0.08
T7270_00796_1	151.4	1.5	152.4	-1.0	81.1	11.88	...	0.44	0.08
T7524_00065_1	353.2	1.2	353.8	-0.6	130.1	11.37	...	0.55	0.14
T7535_00160_1	356.6	1.4	358.8	-2.2	99.7	11.43	10.22	0.56	0.08
T9527_00088_1	-102.2	2.1	-89.6	-12.6	89.9	11.99	10.57	0.62	0.13
C0314269-375257	69.3	1.8	72.9	-3.6	83.8	11.97	12.38	0.48	0.13
C2118490-174605	-125.9	3.1	-133.2	7.3	67.7	11.54	12.37	0.66	0.15
C2234046-564051	-12.0	2.0	-15.2	3.2	77.8	11.88	12.05	0.51	0.12
C2330284-410842	51.6	2.0	48.8	2.8	92.6	11.36	11.51	0.46	0.07
T7006_01317_1	82.6	2.8	81.5	1.1	77.3	11.68	...	0.39	0.03

Table 10. List of RAVE targets in the Geneva-Copenhagen survey. This table presents the Geneva-Copenhagen data together with RAVE measurements. DENIS and 2MASS photometry are reported for convenience. Objects flagged with (*) are binary stars and are discarded from the analysis.

Identifier	RAVE		GENEVA		Rad. Vel. diff. (km/s)	V_T/I (mag)	I_{DENIS} (mag)	$J-H$ (mag)	$H-K$ (mag)
	Rad. Vel.	Rad. Vel.	Rad. Vel.	Rad. Vel.					
	(km/s)	error (km/s)	(km/s)	error (km/s)					
T8468_01019_1	8.7	1.3	8.2	0.3	0.5	9.95		0.36	0.10
T6053_00177_1	57.9	1.4	55.4	0.7	2.5	11.56	10.39	0.59	0.10
HD 143885	1.7	1.3	-0.3	0.2	2.0	7.66	8.82	0.24	0.07
HD 146124	14.2	2.2	10.8	0.2	3.4	6.85		0.31	0.14
HD 153713	-4.7	1.8	-6.8	0.3	2.1	8.54	9.04	0.45	0.10
HD 154550(*)	-7.3	1.7	-7.4		0.1	8.18	8.77	0.24	0.03
HD 155221	-49.3	1.4	-49.7	0.2	0.4	7.80	9.17	0.31	0.11
HD 155755	-0.3	1.5	-2.4	0.4	2.1	7.91		0.23	0.07
HD 156741(*)	-51.4	1.3	-52.5	0.2	1.1	8.39	8.67	0.35	0.09
HD 157316	-1.9	1.9	-1.3	0.9	-0.6	6.26	8.80	0.19	0.05
HD 157387	24.5	1.1	24.8	0.3	-0.3	7.25	7.61	0.21	0.06
HD 157887	-20.7	1.2	-20.7	0.2	0.0	7.67	8.44	0.29	0.08
T8454_00006_1	7.8	1.5	4.3	0.2	3.5	10.18		0.38	0.08

